

1 **IITM High-Resolution Global Forecast Model Version 1: An attempt**  
2 **to resolve monsoon prediction deadlock**

3 R. Phani Murali Krishna<sup>1</sup>, Siddharth Kumar<sup>1</sup>, A. Gopinathan Prajeesh<sup>2</sup>, Peter Bechtold<sup>3</sup>, Nils Wedi<sup>3</sup>,  
4 Kumar Roy<sup>4</sup>, Malay Ganai<sup>1</sup>, B. Revanth Reddy<sup>1</sup>, Snehlata Tirkey<sup>1</sup>, Tanmoy Goswami<sup>1</sup> , Radhika  
5 Kanase<sup>1</sup>, ~~and~~ [Sahadat Sarkar<sup>1</sup>](#), [Medha Deshpande<sup>1</sup>](#), Parthasarathi Mukhopadhyay<sup>1,5</sup>  
6

7 <sup>1</sup>Indian Institute of Tropical Meteorology, Ministry of Earth Sciences, Dr. Homi Bhabha Road, Pune 411008, India

8 <sup>2</sup> King Abdullah University of Science and Technology, Saudi Arabia

9 <sup>3</sup> ECMWF

10 <sup>4</sup> University of Victoria, Canada

11 [5 Department of Earth and Environmental Sciences, Indian Institute of Science Education and Research, Berhampur 760003,](#)  
12 [Odisha, India](#)  
13  
14  
15

16 *Correspondence to:* Dr. P. Mukhopadhyay (mpartha@tropmet.res.in; [parthasarathi64@gmail.com](mailto:parthasarathi64@gmail.com))  
17  
18  
19  
20  
21  
22  
23  
24  
25

26

27

28 **Abstract.** The prediction of Indian monsoon rainfall variability affecting a country with a population of billions remained  
29 one of the major challenges of the numerical weather prediction community. While in recent years, there has been a  
30 significant improvement in predicting the synoptic scale transients associated with the monsoon circulation, the intricacies of  
31 rainfall variability remained a challenge. Here, an attempt is made to develop a global model using a dynamic core of a cubic  
32 octahedral grid that provides a higher resolution of 6.5 km over the global tropics. This high-resolution model has been  
33 developed to resolve the monsoon convection. Reforecasts with the IITM High-resolution Global Forecast Model (HGFM)  
34 have been run daily from June through September 2022. The HGFM model has a wave number truncation of 1534 in the  
35 cubic octahedral grid. The monsoon events have been predicted with a ten-day lead time. The HGFM model is compared to  
36 the operational GFS T1534. While the HGFM provides skills comparable to the GFS, it shows better skills for higher  
37 precipitation thresholds. This model is currently being run in experimental mode and will be made operational.

38

39

40

41

42

43

44

45

46

47

48

49

50

51

52

53

54

## 55 1 Introduction

56 In spite of significant improvement in numerical weather prediction skill in the last decades (Bechtold et al., 2008;  
57 Magnusson and Kallen 2013; Hoffman et al., 2018) predictions of tropical rainfall variability remain a challenge (Westra et  
58 al., 2014; Prakash et al., 2016). Stephens et al. (2010) demonstrated that the models predict in the tropics too many rainy  
59 days which are in the lighter rain category. The challenges of tropical rainfall variability have also been demonstrated by  
60 Watson et al., 2017. The vagaries of the Indian monsoon every year affect the lifestyle of billions of people and the economy  
61 of the Indian sub-continent modulating its Gross Domestic Product (GDP) (Gadgil and Gadgil, 2006). It is therefore of the  
62 utmost importance to improve the weather prediction skill in general and extreme precipitation events in particular. With the  
63 increase of computing power, the resolution of numerical weather prediction models have been increasing and global models  
64 with a resolution of 1~7 km have become a reality ([Majewski et al., 2002](#); [Satoh et al., 2005](#); Miura et al., 2007; [Satoh et al.,  
65 2005](#); [Staniforth and Thuburn, 2012](#); [Li et al., 2015](#); Satoh et al., 2019; Wedi et al., 2020). The higher resolution of  
66 Numerical Weather Prediction (NWP) models has been found to produce a realistic rainfall variability across scales  
67 including diurnal variation, better Madden Julian Oscillation (MJO) variability and seasonal mean climate (Kinter et al.,  
68 2013; Rajendran and Kitoh, 2008; Skamarock et al., 2012; Molod et al., 2015; Crueger et al. 2018; Giorgetta et al., 2018). In  
69 India, operational NWP was initiated with moderate resolution of T80 and then gradually enhanced to T382, T574 (Prasad  
70 et al., 2011, 2014, 2017) and very recently to T1534 (Mukhopadhyay et al., 2019). The advantage of using higher resolution  
71 (T1534~12.5 km) as against the lower resolution T574 (~27 km) was found by enhancement of the model skill by 2 days  
72 (Rao et al., 2019). The National Centre for Environmental Prediction (NCEP) GFS model with 21 members has been used  
73 for probabilistic forecasts since June 2018 (Deshpande et al., 2021). The high-resolution GFS T1534 is found to enhance the  
74 skill of heavy rainfall event (Mukhopadhyay et al., 2019), tropical cyclones and even block level prediction of rainfall (block  
75 is a sub-division of a districts in India, typically of the size of the grid of GFS T1534). However, the skill of the GFS T1534  
76 for prediction of extremely heavy precipitation can still be improved particularly over the orographic regions of India such as  
77 the southern coastal state of Kerala, India (Mukhopadhyay et al., 2021).

78 The 12-km deterministic and the ensemble model based on the GFS do show reasonably good skill in capturing the monsoon  
79 rainfall with 3 to 5 days lead time. The skill of the GFS forecast for Indian monsoon has been reported by Mukhopadhyay et  
80 al. (2019) and the skill of tropical cyclones with the Global Ensemble Forecast System (GEFS) has also been reported in  
81 [Deshpande et al. \(2021\)](#) [and Kanase et al. \(2023\)](#). However, in a recent study Mukhopadhyay et al. (2021) showed that three  
82 state-of-the-art ensemble forecast systems namely the GEFS, the United Kingdom Meteorological Office (UKMO) based  
83 NCMRWF Ensemble Prediction System (NEPS) run by National Centre for Medium Range Weather Forecasting  
84 (NCMRWF) and the Integrated Forecasting System (IFS) by ECMWF struggled to capture the extremely heavy rainfall over  
85 Kerala state of India during August 2018 and August 2019 extremely heavy rainfall episode. This in fact brought up the  
86 limitation of the model in resolving the rainfall variability over the Indian region and more importantly over the orographic  
87 region. One of the limitations in resolving the regional variabilities of rainfall is the horizontal resolution which does not

88 allow the model to resolve the smaller scale processes. Therefore, a need was felt to enhance the horizontal resolution of the  
89 existing GFS based forecasting system. As running of a model close to the convection permitting model (at a resolution  
90 lesser than 10 km) is computationally too expensive in conventional linear reduced Gaussian grids, it was thought to build a  
91 weather model with a grid which has a variable resolution from the pole to the equator. In view of this, ~~the Tco has been~~  
92 ~~identified and~~ the GFS linear reduced Gaussian Grid at triangular truncation 1534 is replaced by an equivalent truncation of  
93 1534 in triangular cubic octahedral (Tco) grid. The equivalent model resolutions of the linear T1534 and the cubic Tco1543  
94 grids are displayed in Fig. 1a. Indeed, as the linear grid has a roughly uniform grid point resolution of 12.5 km the octahedral  
95 grid has a resolution of about 8 km in the Polar Regions and around 6 km in the tropical band. One of the prominent  
96 examples of the Global NWP model with the Tco grid is that of the European Centre for Medium-Range Weather Forecasts  
97 (ECMWF) model suites. The Tco grid provides several advantages (ECMWF Documentation Cy43r1, 2016) over that of the  
98 conventional reduced Gaussian linear grid (Fig. 1a), to name a few- significant reduction in computation cost, improved  
99 representation of orography, better filtering and better conservation properties. These properties of Tco make it a better  
100 candidate, particularly for the utilization of high-performance computers (HPC).

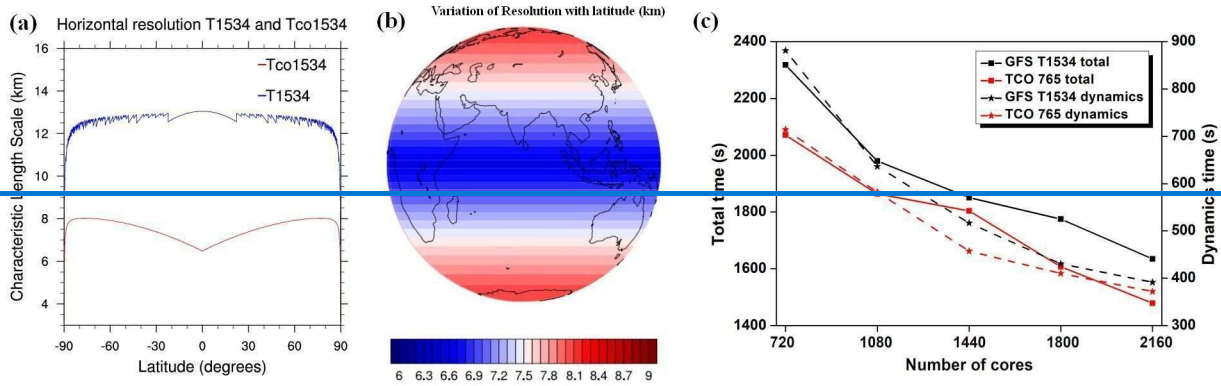
101 This paper is the first attempt to best of our knowledge, towards building a model close to a convection permitting global  
102 weather model in India with an emphasis to Indian monsoon rainfall variability. The details of the model development and  
103 the experiments conducted have been elaborated in Sect. 2. The model results are analysed in Sect. 3, and the conclusion of  
104 the study is summarized in Sect. 4.

## 105 **2 Model, Data and Methodology**

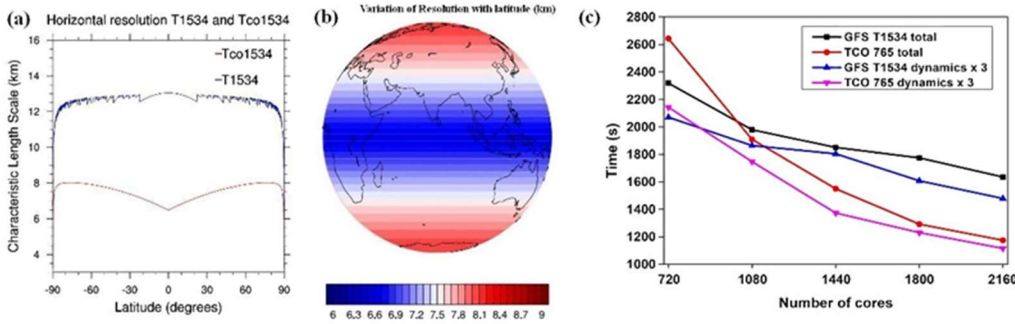
106 This [A](#) new grid, namely the Triangular Cubic Octahedral (Tco) grid, has been adopted to change the existing GFS (semi-  
107 lagrangian) Gaussian linear model system. In the spectral domain, dynamical fields are represented by the sum of spherical  
108 harmonics. The total wavenumber characterizes the spherical harmonics, and the associated wavelength is the ratio of the  
109 circumference of the Earth to the total wavenumber. The value of the maximum wavenumber ( $n_{max}$ ) used to represent a  
110 field as the sum of spherical harmonics is also the spectral truncation of the model. In the case of both GFS and Tco, the  
111 value of  $n_{max}$  is 1534. For the same spectral truncation  $n_{max}$ , the number of latitude circles from the equator to the pole  
112 can vary depending on the choice of spectral transformation. For a linear grid,  $n_{max}=2N-1$ , and for a cubic grid,  $n_{max}=N-$   
113  $1$ . Therefore, for a linear Gaussian grid, the smallest wavelength is represented by only two grid points, as is the case with  
114 the GFS 1534 model. However, in the case of triangular truncation, the smallest wavelength is represented by four grid  
115 points (in the case of the Tco grid). In triangular truncation, for the same spectral truncation, the number of latitude circles is  
116 about double that of the linear truncation. For the GFS model, the horizontal resolution is  $\sim 12.5$  km, and applying the cubic  
117 grid ensures that the horizontal resolution becomes  $\sim 6.5$  km in the tropics (about half of the currently used model resolution)  
118 for the Tco grid. In the Tco grid, the number of latitude circles is 1535.

119 Once a particular choice of spectral truncation is made, the number of latitude circles becomes obvious. However, the  
120 number of longitude circles per latitude circle remains to be prescribed for the creation of the global grid structure. In a fully  
121 Gaussian grid, the number of longitude circles per latitude circle remains the same throughout the latitudes from the equator  
122 to the pole. Thus, the effective resolution near the poles becomes very high compared to the equatorial regions. This specific  
123 requirement demands too many computational resources and poses problems of numerical instability. To overcome that, in  
124 the linear Gaussian grid, the number of latitude circles decreases in a certain way from the equator toward the pole to ensure  
125 almost the same zonal resolution. For the cubic octahedral grid, the number of longitude points per latitude circle is  
126 prescribed in a different way. The latitude circle closest to the pole consists of 20 longitude points, and the number of  
127 longitude points increases by 4 at each latitude circle, moving from poles towards the equator. The number of longitude  
128 points at the equator in the case of the Tco grid is given by  $N_x=20+1534*4=6156$ . Therefore, the zonal grid  
129 length= $2\pi*R/N_x\sim 6.5$  km. In the original reduced Gaussian grid, the number of longitude points per latitude remains fixed in  
130 different blocks of latitudes. The number of latitude points jumps from one block to the other by a constant number. Unlike  
131 the linear reduced Gaussian grid, the horizontal resolution varies more smoothly with latitudes in Tco. The Collignon  
132 projection of a sphere obtains this configuration onto an octahedron. In the current study, the Tco grid at truncation  
133 wavenumber of 1534 is being used. [This new version of the model is mentioned as HGFM \(High-resolution Global Forecast](#)  
134 [Model Version 1\) throughout the manuscript.](#) Fig. 1a and Fig. 1b depicts the variation of grid resolution with latitude in the  
135 GFS (SL) and HGFM (Tco).

136 Before testing the HGFM with complete physics (see Table 1 for description of physics being used in both versions of  
137 model), we have made a version of HGFM with only a dynamical core following Held and Suarez (1994), referred to as  
138 HS94. The HS94 is run to check the stability of the Tco grid framework. Surface boundary conditions for the Tco grid have  
139 been meticulously prepared to ensure the accuracy of grid-point representation. Moreover, the HGFM (Tco1534) has been  
140 developed with complete physics and incorporates essential boundary conditions, including global topography, global land-  
141 use-land-cover etc. The HGFM at Tco1534 truncation is depicted over the globe in Fig. 1. The model has been run daily for  
142 a ten days forecast at IITM Pratyush HPC system. To understand the computational efficiency of Tco model, time taken for  
143 one day forecast is compared for GFS 1534 and HGFM model (Tco 765 in this case) (see Fig. 1c). A comparison between  
144 GFS 1534 and Tco 765 is made because both models have almost same number of grid points. It is clear that Tco 765  
145 significantly saves the runtime in dynamical core and total time as well. Moreover, [the](#) Tco model is in general more scalable  
146 for higher number of cores (not shown). The model has been run [since 2022 and here the analyses](#) for the summer monsoon  
147 season of June, July, August and September (JJAS) 2022 [are being presented](#). A detailed analysis of the model run [has](#)  
148 [been](#) discussed in the results section. Apart from the monsoon season [\(JJAS 2022\)](#), few case studies [have](#) also [been](#)  
149 discussed.



150



151

152 **Figure 1. Variation of grid length with latitude in GFS (blue) and Tco (red) (a), depiction of grid resolution over the globe in Tco**  
 153 **grid (b), total and dynamics time taken for different number of cores (c). Time taken by GFS and HGFM for one day forecast**  
 154 **(Left vertical axis is total time taken and right axis represents time taken by model dynamics time multiplied by 3).**

155 To verify the model forecast, the daily observed gridded rainfall data from the Integrated Multi-satellite Retrievals for GPM  
 156 (IMERG) version 06B (Huffman et al., 2019) rainfall data at  $0.1^\circ \times 0.1^\circ$  (10 km) horizontal resolution is utilized for the year  
 157 of 2022 for JJAS season. Additionally, to validate a heavy rainfall event over India, gridded rainfall from India  
 158 Meteorological Department (IMD) at 25 km resolution is used. The IMD rainfall data are merged product of gridded rain  
 159 gauge observations and GPM satellite-estimated rainfall over the ISM region (Mitra et al., 2014). Further, the reanalysis-  
 160 based parameters from the fifth generation of ECMWF atmospheric reanalyses (ERA5) products (Hersbach and Dee, 2016)  
 161 are utilized at 25 km horizontal resolution during JJAS of the year 2022.

162 **Table 1. Details of domain configuration and physics options used in HGFM.**

Physics	Description
Radiation	Rapid Radiative Transfer Model (RRTM) for both Shortwave and Longwave (Iacono et al., 2000; Clough et al., 2005) with Monte Carlo Independent Column Approximation (McICA)
Microphysics	Formulated grid-scale condensation and precipitation (Sundqvist et al., 1989; Zhao and Carr, 1997)

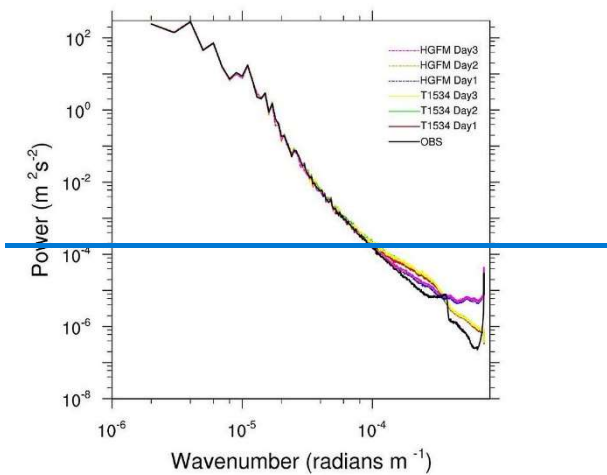
Convection	Aerosol aware and Mass flux based Simplified Arakawa-Schubert (SAS) shallow convection (Pan and Wu, 1995; Han and Pan, 2011; Arakawa and Wu, 2013; Han et al., 2017)
Planetary Boundary Layer (PBL)	Hybrid Eddy-Diffusivity Mass Flux vertical turbulent mixing scheme (Han and Pan, 2011; Han et al., 2016)
Gravity Wave Drag (GWD)	Mountain blocking (Alpert et al., 1988; Kim and Arakawa, 1995; Lott and Miller, 1997) and stationary convective-forced GWD (Chun and Baik, 1998)

163

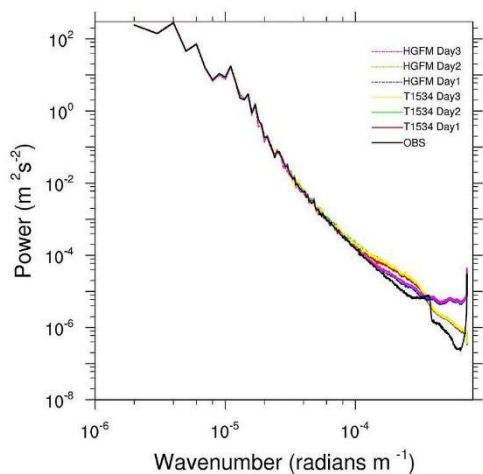
## 164 3 Results and Discussions

### 165 3.1 200 hPa Kinetic Energy Spectra

166 Before going into the details of model validation, the first metric to evaluate the model fidelity is to validate the Kinetic  
167 Energy (KE) spectra of 200 hPa wind. The KE spectra provide information about the distribution of kinetic energy across the  
168 scale. A close resemblance between observed /reanalysis-based spectra and spectra produced by the model gives confidence  
169 about accuracy of overall model configuration. The kinetic energy (KE) spectrum in the upper troposphere exhibits two  
170 clearly defined power-law patterns. From observational studies, it is established that at large-scale, rotational modes prevail  
171 ( $k^{-3}$ ) while at mesoscales, divergent modes are dominant ( $k^{-5/3}$ ) (Nastrom and Gage, 1985). Figure 2 shows the KE spectra of  
172 200 hPa wind simulated by HGFM and GFS T1534. The KE spectra for the forecast up to 3 days lead time has been  
173 compared with ERA5 data. While both the models reasonably capture  $k^{-5/3}$  behaviour of the mesoscale at the higher  
174 wavenumber, but the HGFM appears to capture the  $k^{-3}$  behaviour of the large scale at the lower wavenumber closer to  
175 observation. It is observed that beyond wavenumber  $10^{-4}$  there is slight departure of the spectra from observation specially  
176 for HGFM. However, the regions of interest in KE spectra are the  $k^{-3}$  dependence for the large scale and a less steep,  $k^{-5/3}$   
177 dependence for the mesoscale. The tail of the spectra at higher wave numbers typically has less energy due to the dissipation  
178 of kinetic energy with increase of wave number, however models tend to dissipate the energy at higher wave number at a  
179 much faster rate depending on the damping used in the model (Skamarock, 2004). To keep the spectra realistic, a common  
180 practice is to reduces the damping which may increase the energy at higher wavenumbers as observed in this case for  
181 HGFM. However, this will not have much impact in our analysis as these are the small-scale features. The KE spectra  
182 indicates that overall configuration of both versions of the model is robust. Therefore, now we turn our attention towards  
183 verification of convective available potential energy and rainfall simulations, the most desirable parameter in model  
184 forecasts.



185



186

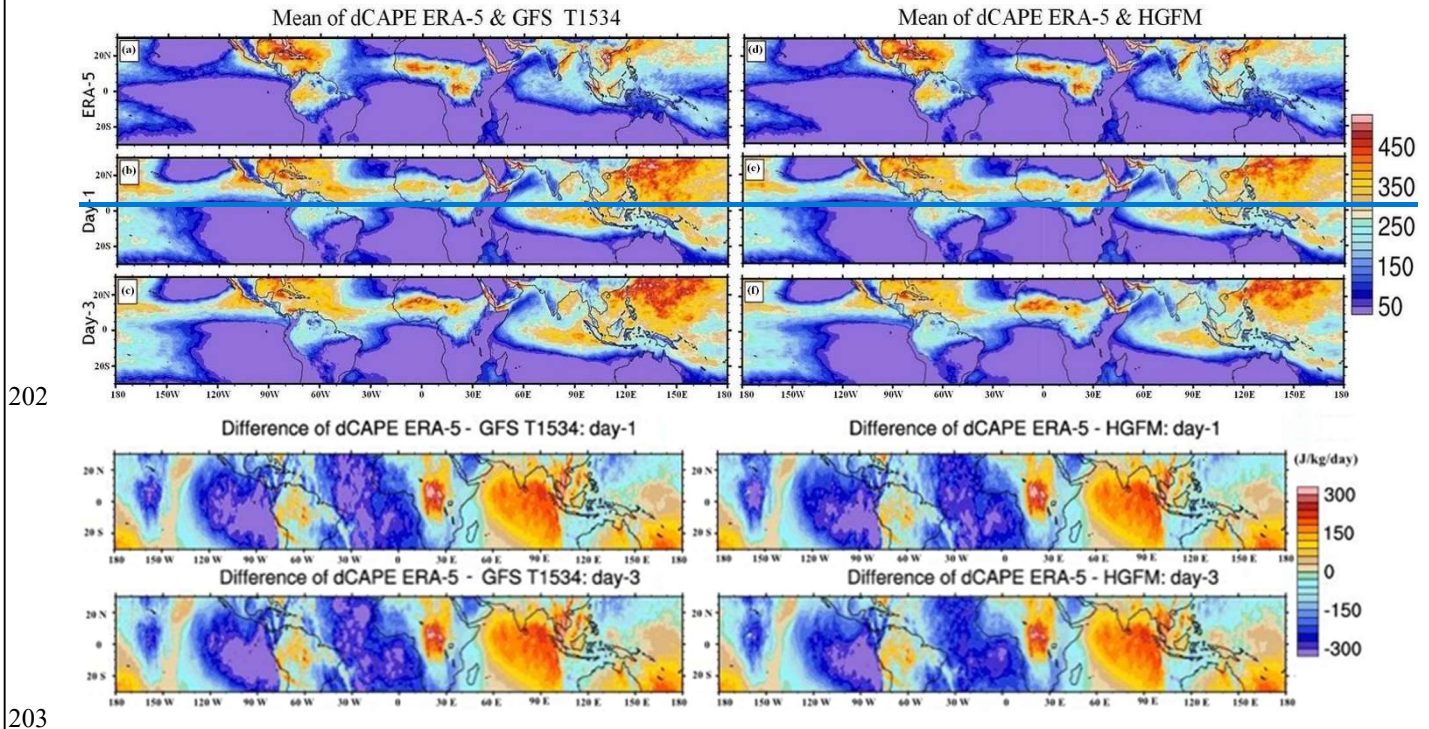
187 **Figure 2. Kinetic energy spectra of 200 hPa wind for observation and different lead times of GFS T1534 and HGFM.**

188 **3.2 Quasi-equilibrium in models**

189 Both model versions are run at high-resolutions, close to convection-permitting models' resolution. However, in this case, a  
 190 scale-aware convection scheme is used to parameterize deep convection in the model. From observational studies it has been  
 191 established that tropical atmosphere deviates significantly from the convective-quasi equilibrium (e.g., Zhang, 2003). The  
 192 convective quasi-equilibrium (CQE) is the fundamental approach used in most models for parameterization of deep  
 193 convection (Arakawa and Schubert 1974). To understand up to what extent both model versions obey CQE, we adopted [the](#)  
 194 methodology suggested in Kumar et al. (2022). The absolute value of changes in Convective Available Potential Energy  
 195 (CAPE) at daily timescales is analysed from GFS T1534 and HGFM models for the year 2022 during JJAS and compared  
 196 with the ERA-5 data ([Figure not shown](#)[Fig-3](#)). Notable changes were observed in the daily dCAPE values between GFS



197 T1534 and HGFM compared to ERA-5. The daily dCAPE values from ERA-5 (Fig. 3a, d) data matches better with the  
 198 HGFM (Fig. 3e, f) than GFS T1534 (Fig. 3b, e) for day 1 and day 3 lead times. The difference of dCAPE between ERA-5  
 199 and models is presented for day-1 and day-3 lead time forecast (Fig. 3). The dCAPE difference quantified from ERA-5 with  
 200 GFS T1534 were  $-49.0570$  (J/kg/day) and  $-47.3799$  (J/kg/day) for day1 and day 3 lead times respectively, similarly with  
 201 HGFM  $-49.1278$  (J/kg/day) and  $-43.7668$  (J/kg/day) for day 1 and day 3 lead times respectively.



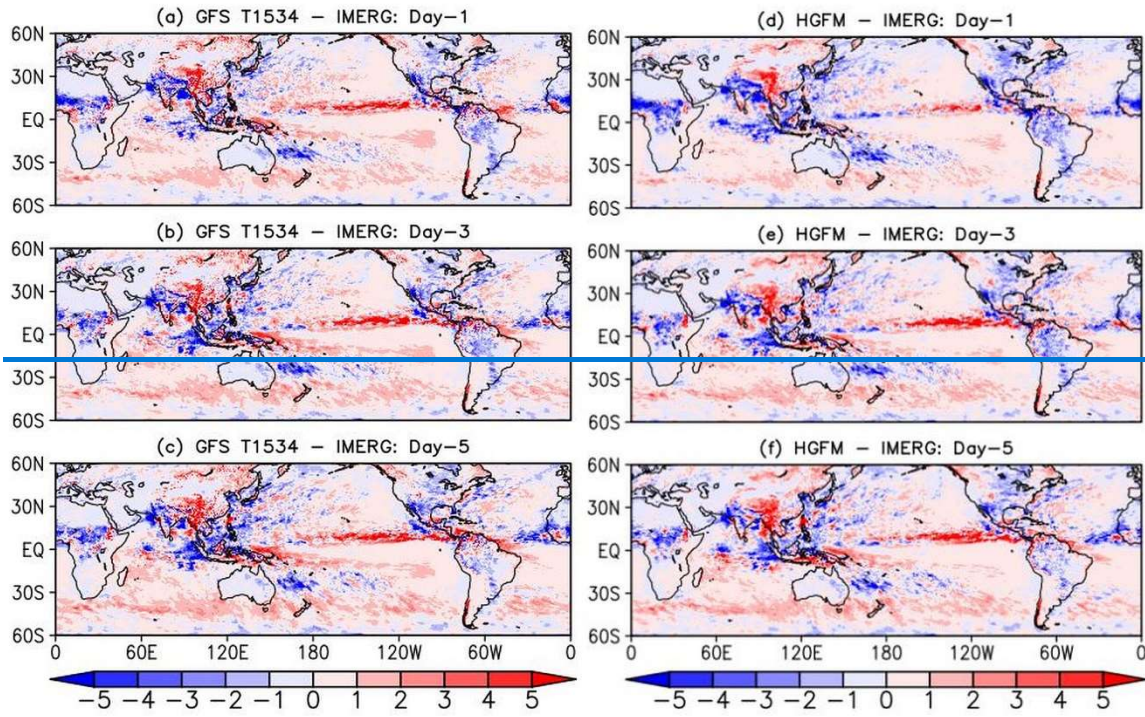
202  
 203  
 204  
 205 **Figure 3. Comparison of dCAPE mean during JJAS 2022 from ERA-5 (a, d) with respect to GFS T1534 (b, c) and TCO 1534 (e, f)**  
 206 **for day-1 and day-3 lead time.**

207 **Figure 3. The difference of dCAPE from ERA-5 and GFS T1534 for day-1 and day-3 (left panels), and from ERA-5**  
 208 **and HGFM for day-1 and day-3 (right panels).**

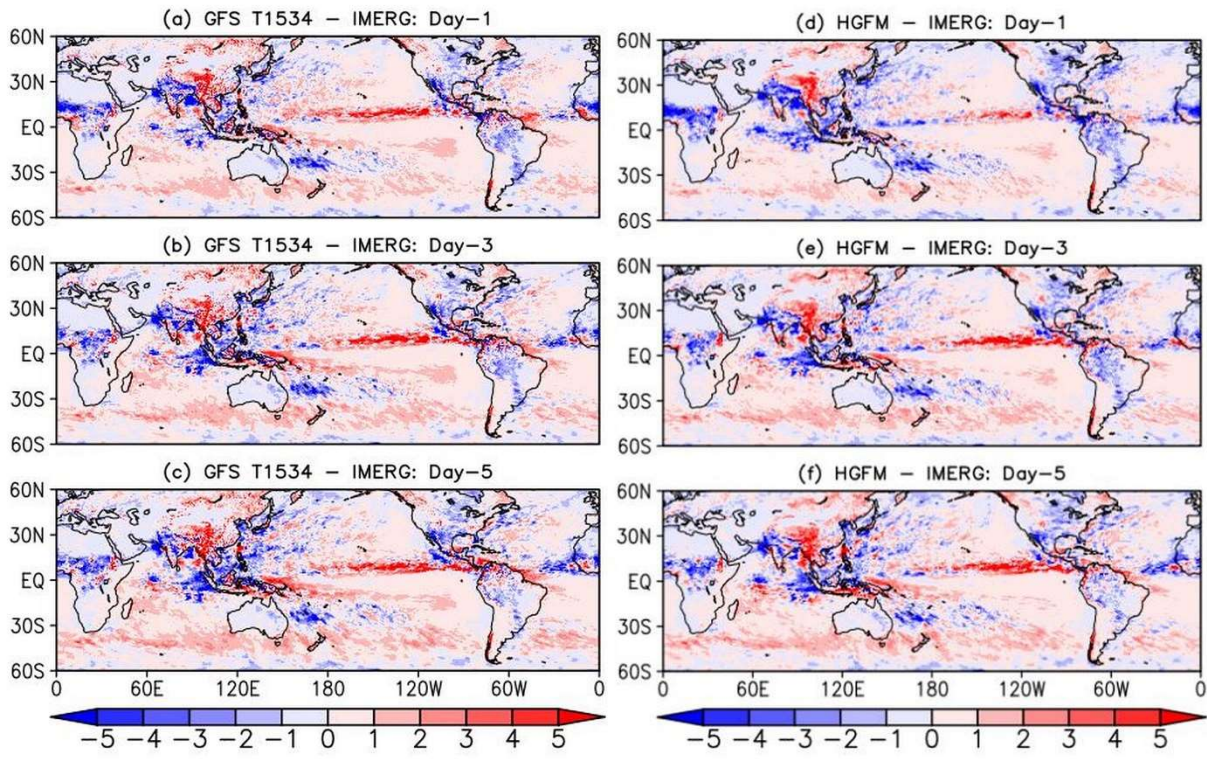
### 209 3.3 Analysis of Global precipitation

210 The global precipitation bias of GFS (left panel of Fig. 4 and HGFM (right panel) with respect to Integrated Multi-satellite  
 211 Retrievals for GPM (IMERG) data, with day 1, day 3 and day 5 lead time is shown in Fig. 4. Both the models broadly show  
 212 a similar rainfall bias over the global land and global ocean. However, there are some subtle differences. The day 1 forecast  
 213 (Fig. 4a) of GFS shows a wet bias over the equatorial eastern Pacific extending up to the tropical western Pacific. On the  
 214 other hand, the HGFM on day 1 lead (Fig. 4d) also shows a wet bias mostly confined over the tropical eastern Pacific and a  
 215 slight negative bias over western Pacific. For HGFM, the positive bias of rainfall over the tropical ocean appears to be

216 mostly over the eastern Pacific while that of GFS appears to be over eastern Pacific and extending towards the central and  
217 west Pacific for all the lead time. The eastern Pacific precipitation overestimation could be due to improper representation of  
218 shallow convection over the region. Raymond (2017) highlighted the complex nature of SST and associated cloudiness and  
219 convection over the region. Apart from the oceanic region, the major global land regions (central African Continent,  
220 Maritime continent, Indian summer monsoon region, northern part of South America) shows a negative bias in both the  
221 models at different lead times (Fig. 4) which is likely related to the model physical parameterizations.



222



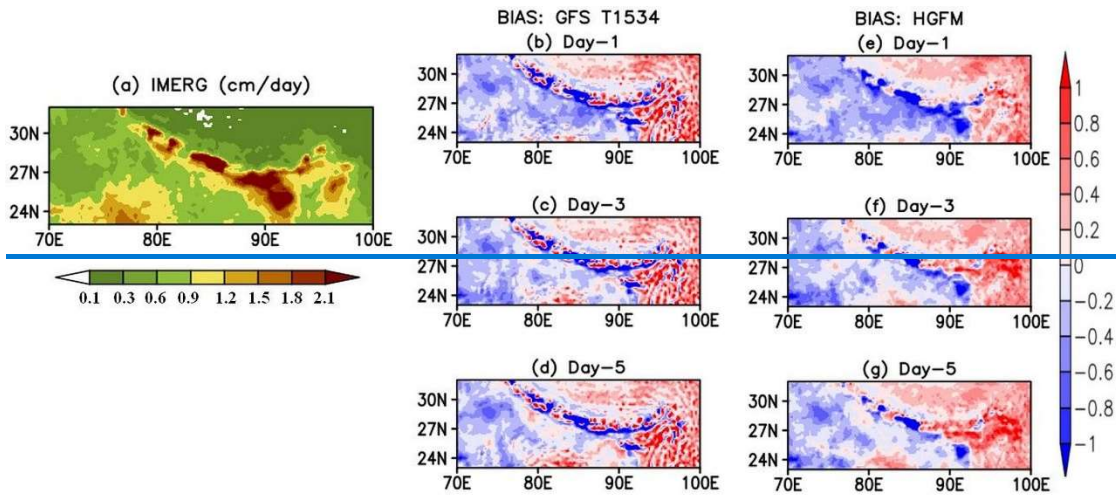
223

224 **Figure 4. Global JJAS precipitation bias ( $\text{mmcm/day-day-1}$ ) of GFS T1534 (left panel) with respect to IMERG for (a) day-1, (b)**  
 225 **day-3 and (c) day-5 lead time. Right column (d-f) indicates similar plots but for HGFM.**

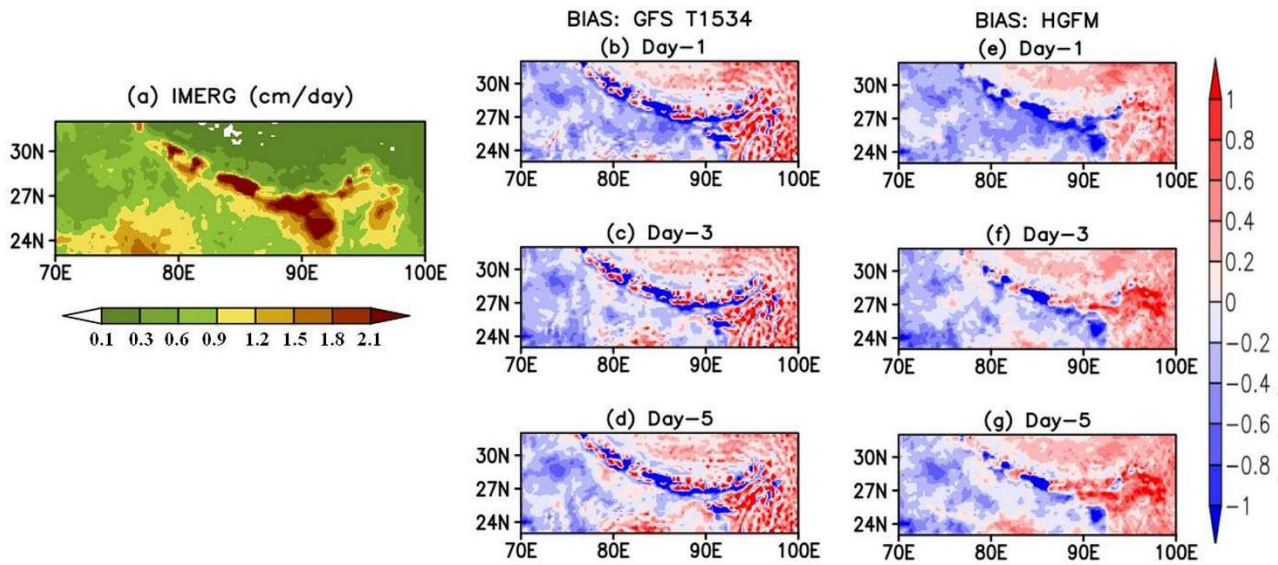
### 226 3.4 Indian summer monsoon precipitation and related features

227 While Fig. 4 depicted the precipitation bias over the global domain, it will be interesting to investigate the model forecast  
 228 performance over the complex orographic region over the Indian domain, the region of our utmost interest. As mentioned  
 229 earlier, one of the major advantages of using a Tco grid is a better representation of orography. Therefore, it is imperative to  
 230 investigate the forecast skill of the high resolution HGFM model over the mountainous Himalayan foothills, adjoining  
 231 northeast India, and Western Ghats (WGs) region (shown in Fig. 5 and 6 respectively). The GFS T1534 model forecasts  
 232 indicate spurious rainfall activity over the Himalayan foothills and northeast India region for all lead times (Fig. 5b-d). On  
 233 contrary, the HGFM model with finer horizontal resolution largely resolves the spurious rainfall over the region as shown in  
 234 Fig. 5e-g. The Gibbs waves are largely suppressed over the mountainous terrains in HGFM compared to GFS T1534.  
 235 Similarly, the precipitation distribution over the WGs region shows considerable overestimation in GFS T1534 for all lead  
 236 times (Fig. 6b-d). On the other hand, the magnitude of overestimation is decreased considerably in HGFM forecasts as  
 237 depicted in Fig. 6e-g. Thus, the above analysis brings out the fact that HGFM shows its potential in predicting realistic  
 238 rainfall distribution over the orographic regions.

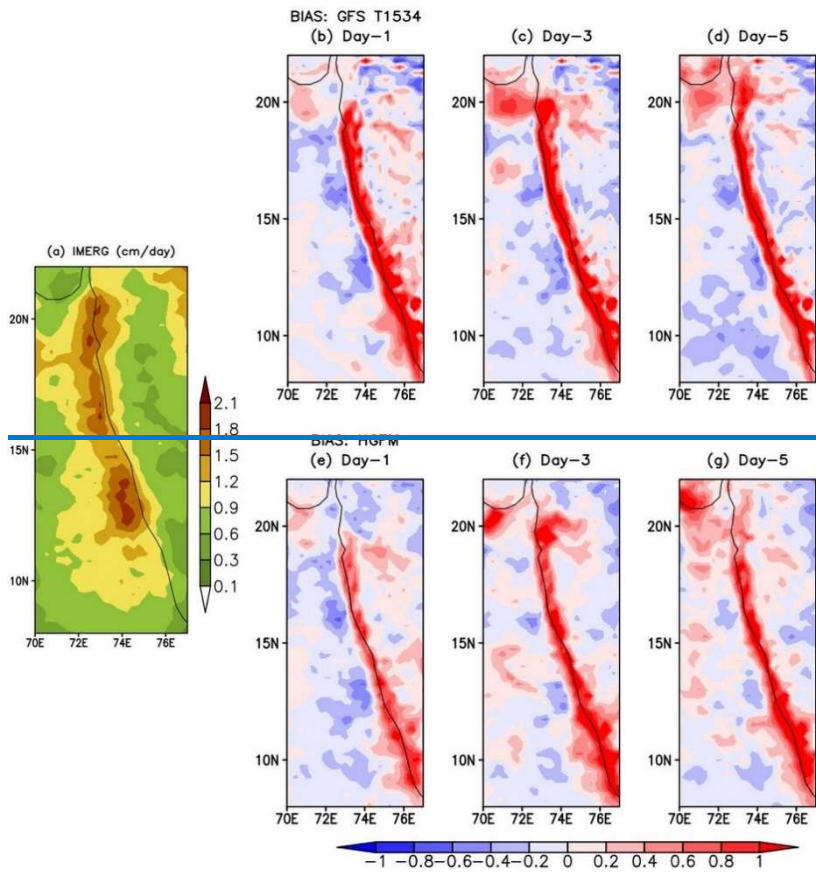
239



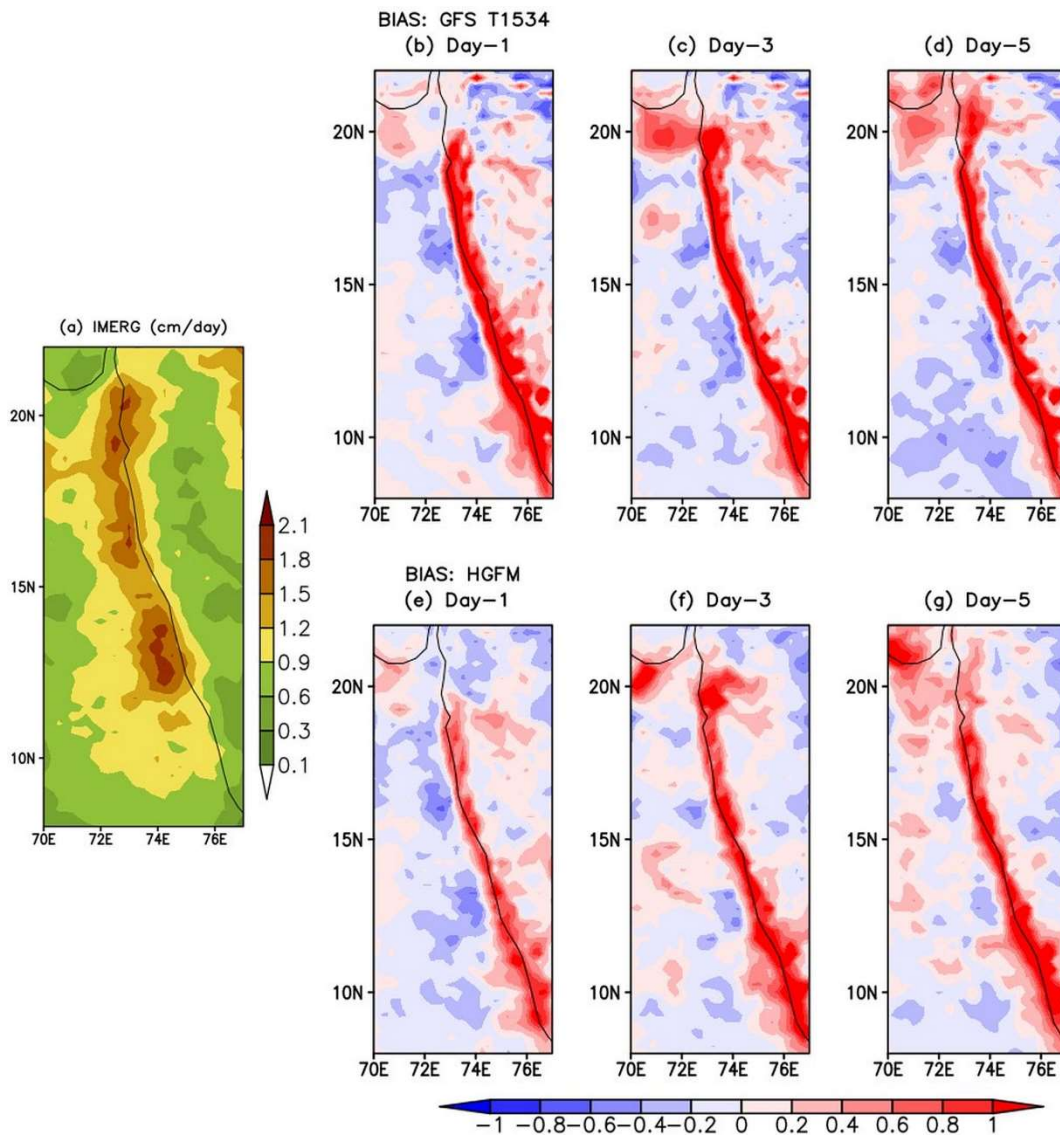
240



241 Figure 5. Comparison of JJAS mean precipitation (mm/cm/day) and Bias in IMERG data (cm/day) (a) with GFS T1534 (b, c, d)  
242 and TCO 1534 (e, f, g) during 2022 over Himalayan foothills and Northeast India for day-1 day-3 and day-5 lead time.



243



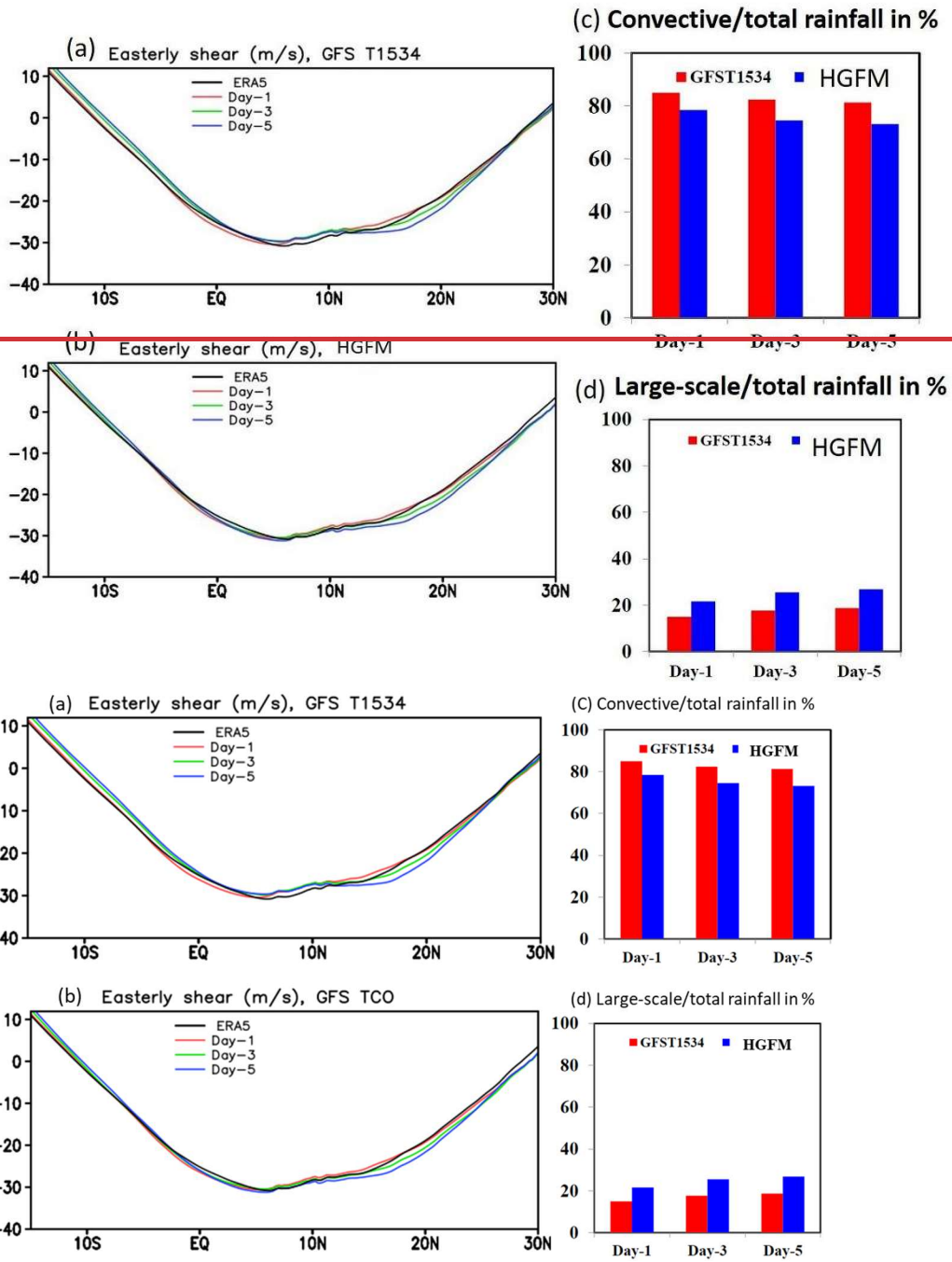
244

245 **Figure 6. Comparison of JJAS mean precipitation (mm/day) and Bias in IMERG data (cm/day) (a) with GFS T1534 (b, c, d)**  
 246 **and TCO 1534 (e, f, g) during 2022 over Western ghats region for day-1 day-3 and day-5 lead time.**

247 One of the prominent features of ISM is [the](#) vertical shear of zonal wind. Previous studies (Jiang et al., 2004; Abhik et al.,  
 248 2013) demonstrated that the vertical easterly wind shear plays a crucial role in inducing baroclinic vorticity ahead of  
 249 northward propagation of summer intra-seasonal oscillation. In order to find out the model forecast skill in predicting  
 250 realistic easterly wind shear (difference between zonal wind at 200 and 850 hPa) during summer monsoon season of 2022,  
 251 the vertical wind shear calculated and represented in Fig. 7a and 7b for GFS T1534 and HGFM respectively over the ISM  
 252 region. Figure 7a indicates slightly weaker easterly shear in GFS T1534 compared to ERA5 around 10°N and 0°-15°S for  
 253 all lead times. On the contrary, the HGFM is able to predict more realistic easterly wind shear over above regions as shown

254 in the Fig. 7b. It is noticeable that both models overestimate the magnitude of easterly shear around 20° N for Day-3 and  
255 Day-5 lead times.

256 Another key feature about tropical precipitation is almost equipartition of rainfall into convective and stratiform rain.  
257 Therefore, it is important to investigate whether the relative improvement in the precipitation distribution over the ISM  
258 region in HGFM forecasts is contributed by improved convective and large-scale precipitation. The model forecasted  
259 convective and large-scale rainfall ratios are shown in Fig. 7c and 7d respectively. It is noteworthy that the large-scale or  
260 stratiform rainfall plays an important role in the propagation and maintenance of the tropical intraseasonal convection  
261 associated with its top-heavy heating profile (Fu and Wang, 2004; Chattopadhyay et al., 2009; Deng et al., 2015). The  
262 heating profile associated with stratiform rain also helps in large-scale organization of convection (see for example,  
263 Choudhary and Krishnan, 2011, Kumar et al., 2017). The contribution of convective rainfall to the total rainfall appears to be  
264 more than 80 % in GFS T1534 forecast for all lead times (Fig. 7c). Similar overestimation of convective rainfall in GFS  
265 T1534 is reported by Ganai et al. (2021). The observed convective (large-scale) rainfall ratio is around 55 % (45 %) as  
266 shown in Abhik et al. (2017). The HGFM forecast shows relative improvement in predicting convective and large-scale  
267 rainfall ratio compared to GFS T1534 (Fig. 7c and 7d). The decrease (increase) in convective (large-scale) rainfall  
268 contribution to total rain is noted in HGFM forecast. The finer horizontal resolution in HGFM possibly allows for a more  
269 accurate representation of deep convective due to scale-aware representation.



270

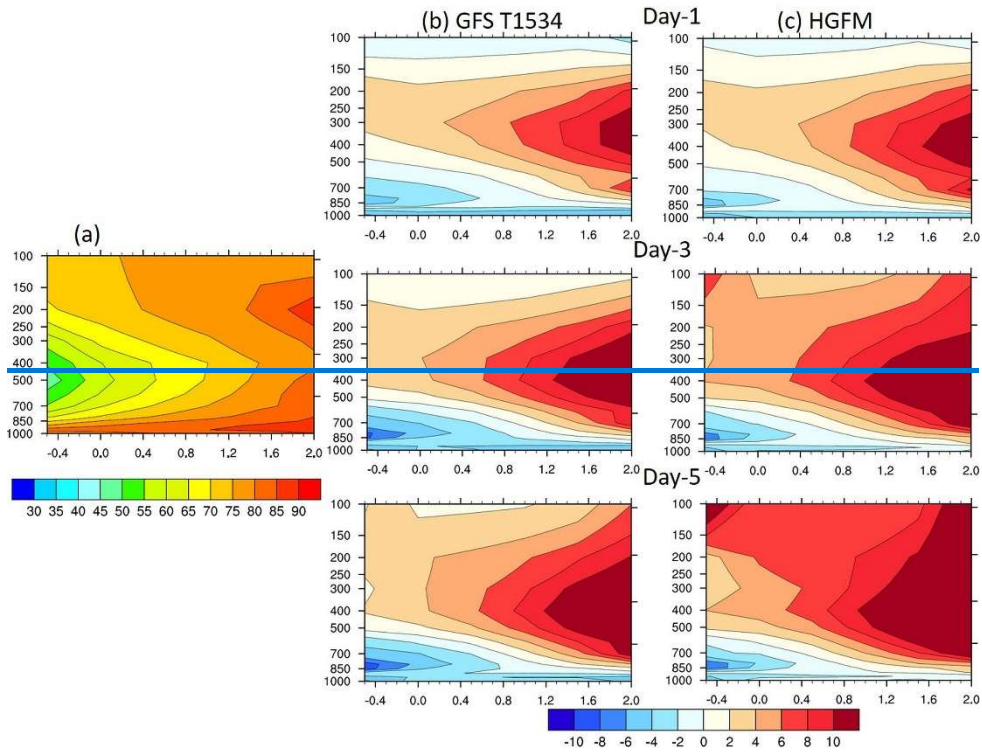
271

272 **Figure 7. Comparison of easterly shear (m/s) from ERA-5 with GFS T1534 (a) and HGFM (b) along with convective/total rainfall**  
 273 **(c) and large scale/total rainfall (d) between GFS T1534 and HGFM during JJAS 2022 for day-1 day-3 and day-5 lead time.**

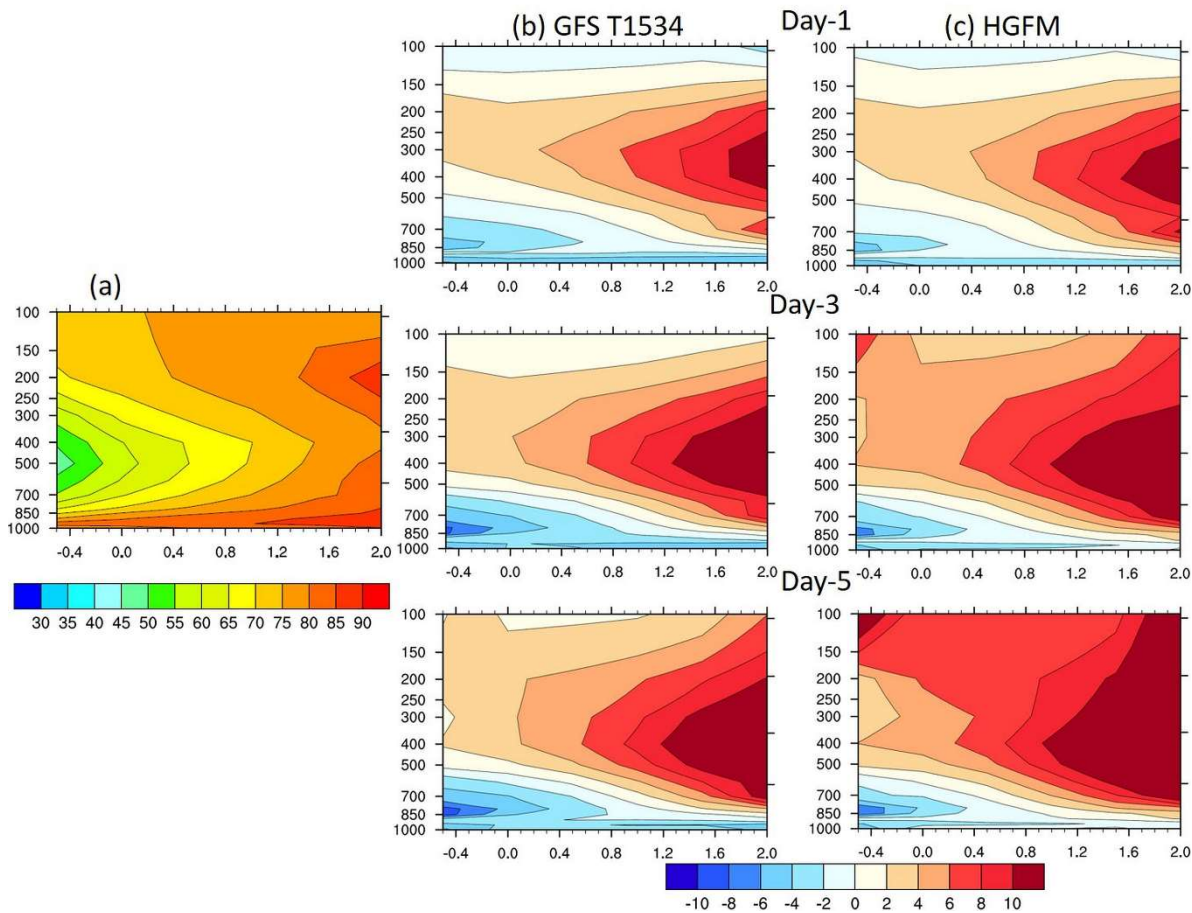
274 To attain further clarity about the model precipitation and moist convective processes, the vertical profile of relative  
 275 humidity as a function of rain rate is analyzed for JJAS of 2022 over the ISM region (60° E-100° E, 10° S-30° N). The bias



276 analysis suggests that GFS T1534 has systematically underestimated the lower-level moisture for all lead times (Fig. 8b). It  
 277 is consistent with the study by Mukhopadhyay et al. (2019) and Ganai et al. (2021) where they reported similar  
 278 underestimation of lower-level moisture over the ISM region ~~in~~ GFS T1534 forecast. In contrast, the HGFM shows  
 279 relative improvement in the lower-level moisture distribution, as depicted in Fig. 4c for all lead times. The enhancement of  
 280 the lower-level moisture is visible as compared to GFS T1534 forecast. However, the upper troposphere is too moist for both  
 281 model forecasts and need further improvement.  
 282 It is observed that overall statistics of monsoon rainfall and related convective processes have significantly improved in the  
 283 HGFM model. In the next section [a case of heavy rainfall is discussed followed by the analysis of some recent tropical](#)  
 284 [cyclone forecasts, are analysed.](#)



285

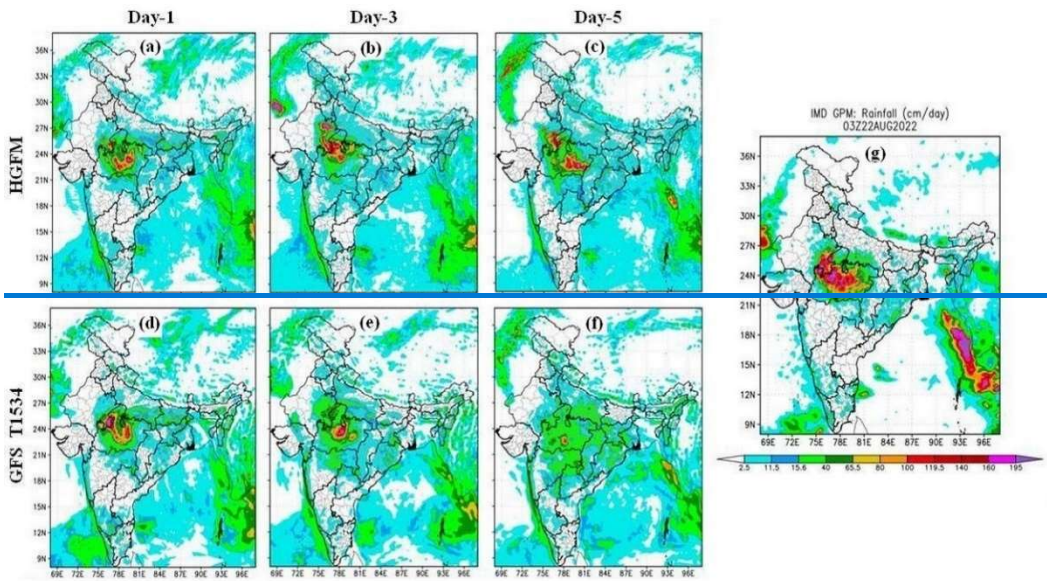


286

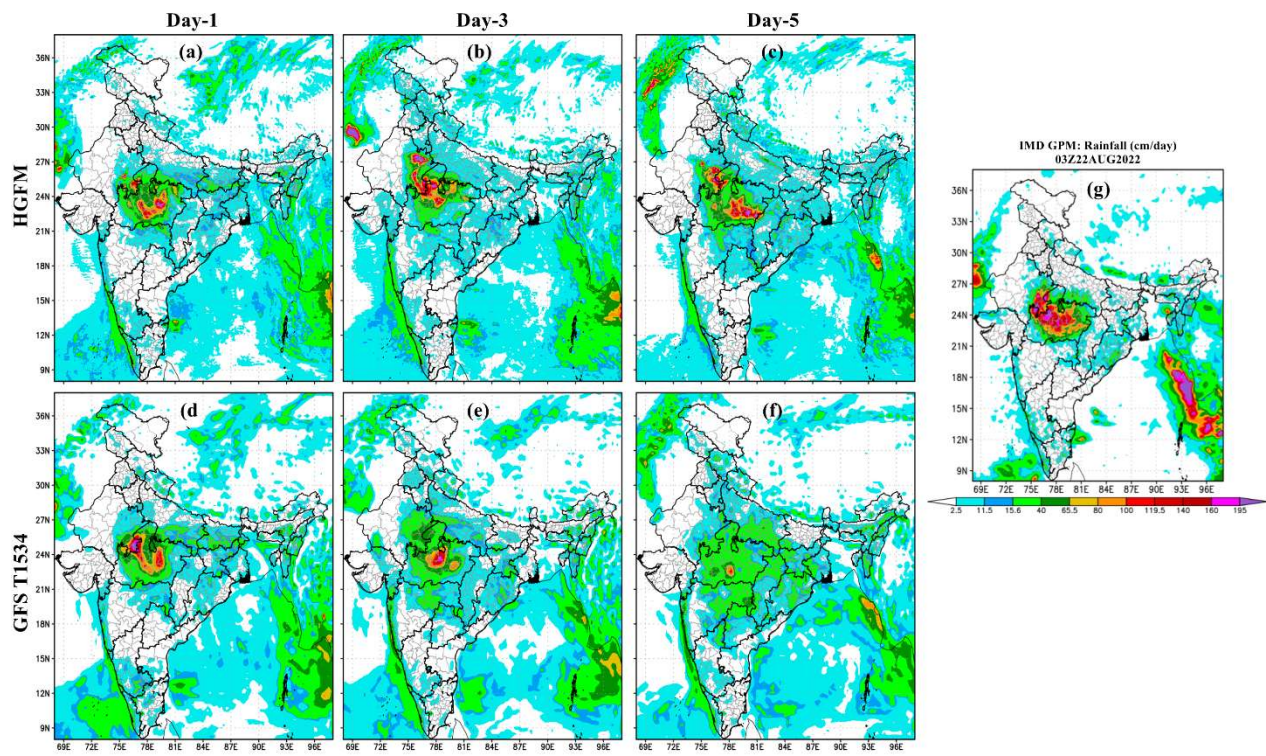
287 **Figure 8. Comparison of Relative humidity (% bias in shaded) vs rain rate (mm/day) over ISM region (60° E-100° E, 10° S-30° N)**  
 288 **during JJAS-2022 from ERA-5 and IMERG (a) with GFS T1534 (b) and HGFM (c) during JJAS 2022 for day-1 day-3 and day-5**  
 289 **lead time.**

### 290 3.5 Evaluation of Heavy Rainfall event

291 A very heavy rainfall event occurred on 22 August 2022 over central India. This event was well captured by both GFS and  
 292 HGFM models as compared to the observed rain from IMD-GPM (shown in Fig. 9). Both HGFM (Fig. 9a, b, c) and GFS  
 293 T1534 (Fig. 9d, e, f) models simulated the heavy rainfall signature compared to IMD GPM (Fig. 9g) on day 1 and day 3  
 294 forecast. However, a major difference was noted for rainfall intensity and spatial distribution on longer lead time (day 5) in  
 295 HGFM and GFS T1534. There is an underestimation of rainfall in both the models compared to observations. Whereas the  
 296 HGFM captures the signal of the occurrence of heavy rainfall even at day 5 lead, which is almost negligible in GFS forecast.  
 297 [Further, the precipitation probability distribution function \(PDF\) is analyzed \(figure not shown\) for the JJAS 2022 monsoon.](#)  
 298 [It is found that the HGFM shows better PDF in the very heavy \(11.56-20.45 cm/day\) and extreme \(>20.45 cm/day\) rainfall](#)  
 299 [category as compared to GFS T1534.](#)



300

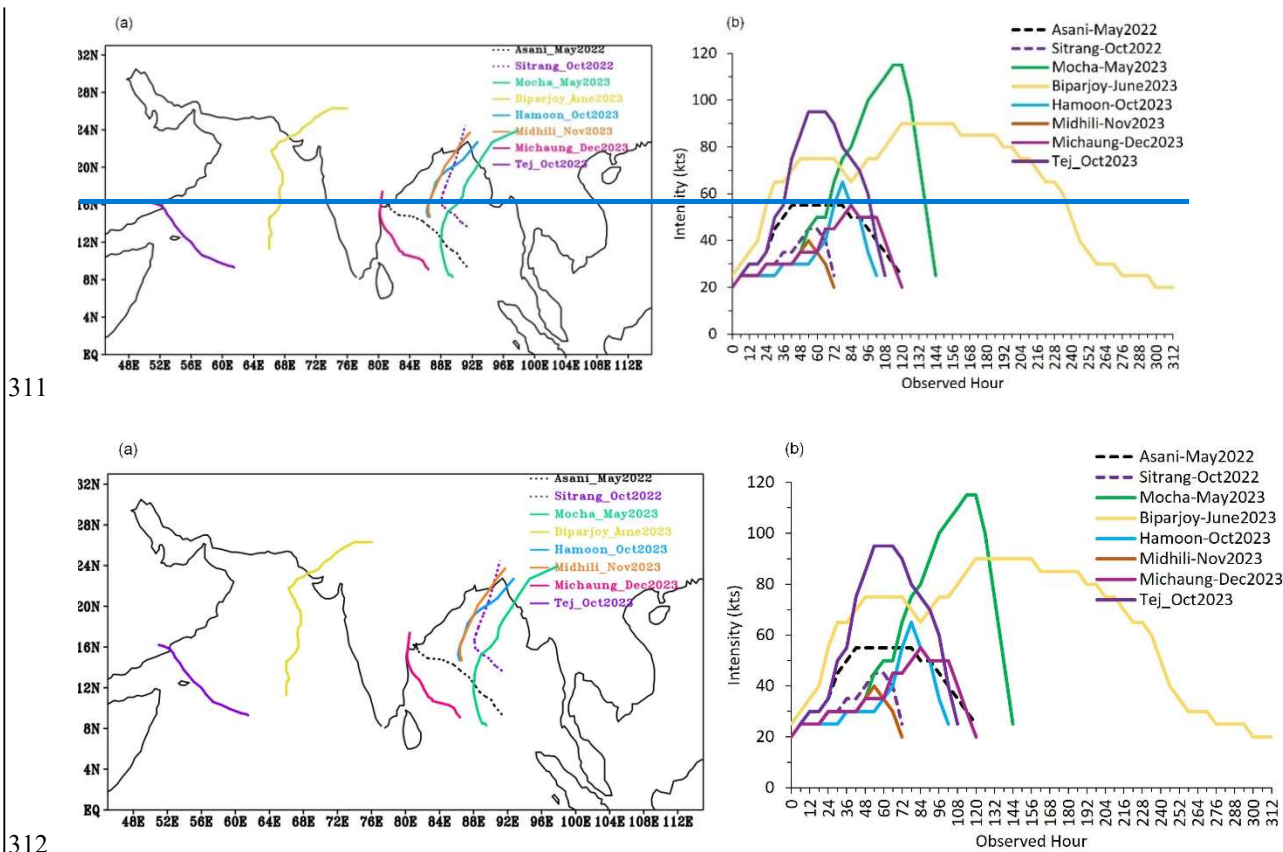


301

302 **Figure 9. Comparison of heavy rainfall event on 22 August 2022 with HGFM (a, b, c), GFS T1534 (d, e, f) for day-1, day-3 and**  
 303 **day-5 lead times with IMD GPM (g) rainfall.**

### 304 3.5 Evaluation of Tropical Cyclone forecast

305 Total eight named cases of tropical cyclones occurred during from 2022 and 2023 (RSMC 2022, RSMC 2023) are  
306 considered in the present study. Out of these 8 cases, 2 cyclones formed over the Arabian Sea and 6 cyclones over the Bay of  
307 Bengal (BOB). The observational best track data of track, intensity and landfall is obtained from IMD and referred as  
308 observations henceforth in the text. Figure 10 shows observed tracks (Fig. 10a) and observed intensity in terms of Maximum  
309 Sustained Wind Speed (MSW Fig. 10b) of the cyclones. The cyclones in the present study have different tracks and various  
310 range of severity in terms of intensity over both the basins.



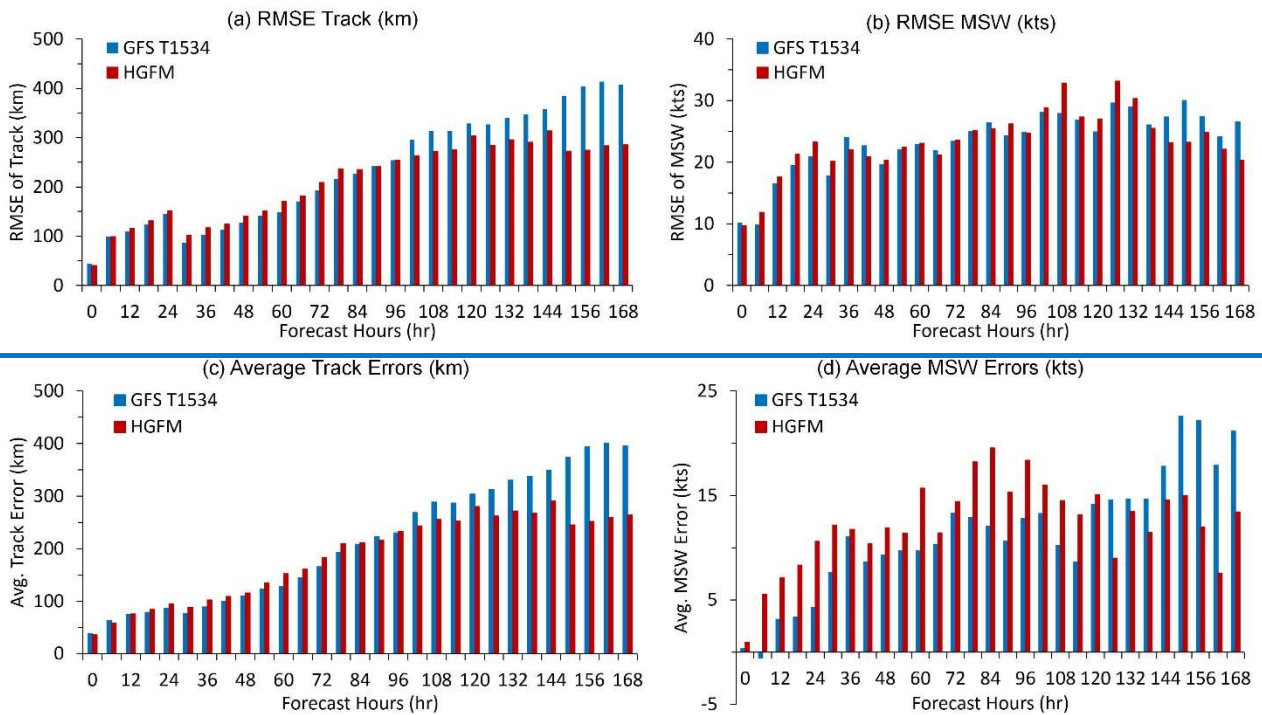
313 Figure 10. a) Observed tracks of the cyclones b) Observed Intensity in terms of Maximum Sustained Wind Speed (kts) during year  
314 2022-2023.

#### 315 3.5.1 Annual Verification of GFS T1534 and HGFM Forecast for tropical cyclone cases during the year 2022 and 316 2023

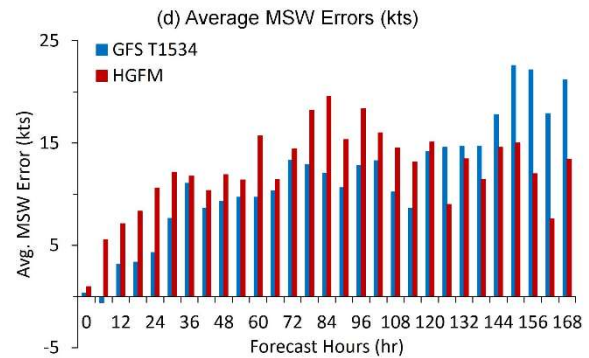
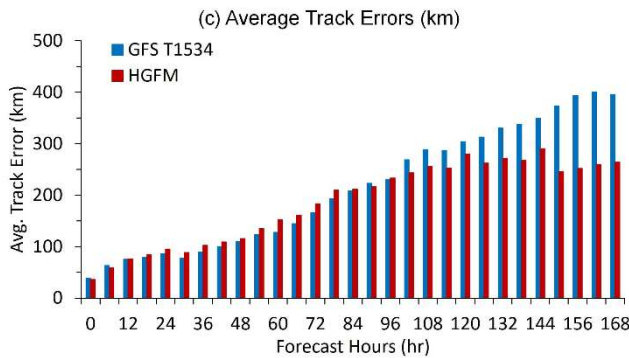
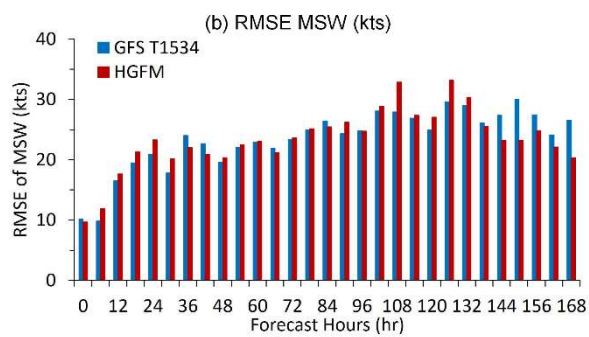
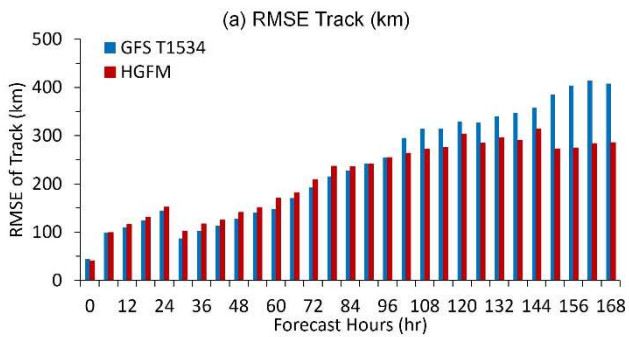
317 For each cyclone case this verification, the lifetime of the cyclone is considered starting from the verification started from the  
318 observed depression stage till observed landfall as per the observation. The total sample includes, For each cyclone case  
319 minimum four (and maximum 10) initial conditions for typical cases are considered depending on the life span of the cases

320 both the models have daily outputs. The errors calculated here are the-averaged for each forecast hour of all such within the  
321 samples for the year 2022 and 2023.

322 The Root Mean Square Error (RMSE) of track and intensity is shown in Fig. 11a- and b respectively. Initially upto 4 days,  
323 GFS T1534 and HGFM performs equally well but the considerable improvement with HGFM is noted after 4 days in both  
324 track and intensity forecast. Figure 11c-d depicts the average track error and average intensity errors for all the cyclones.  
325 The average track errors as well as average intensity errors are reduced drastically in HGFM with longer lead hours (4 days  
326 or more). Average track errors (average intensity errors) are ~300 km (~20 kts) with 7 days leads in HGFM. The average  
327 landfall errors (both position and time) are also evaluated with IMD observations and are shown in Fig. 12. With 4 days lead,  
328 average landfall position errors are ~200 km in HGFM and about 250 for GFS 1534. Overall, the landfall position errors are  
329 less for HGFM, and it reduces further with longer lead. In GFS T1534, landfall position errors are increasing with longer lead  
330 (compared to HGFM). Remarkable improvements are seen in the average landfall time errors in HGFM throughout the life  
331 cycle of cyclones. Overall, the track and intensity forecast are improved with HGFM for longer lead hours (~4 days or  
332 more), which is an added advantage for the early warning and mitigation purpose. Here, one of the cyclone cases (cyclone  
333 Biparjoy) is discussed in detail.

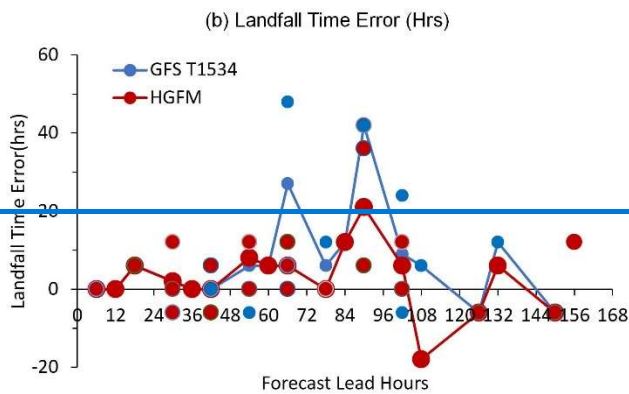
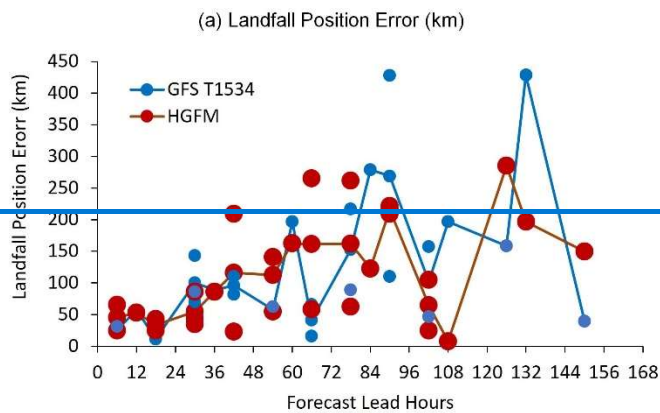


334

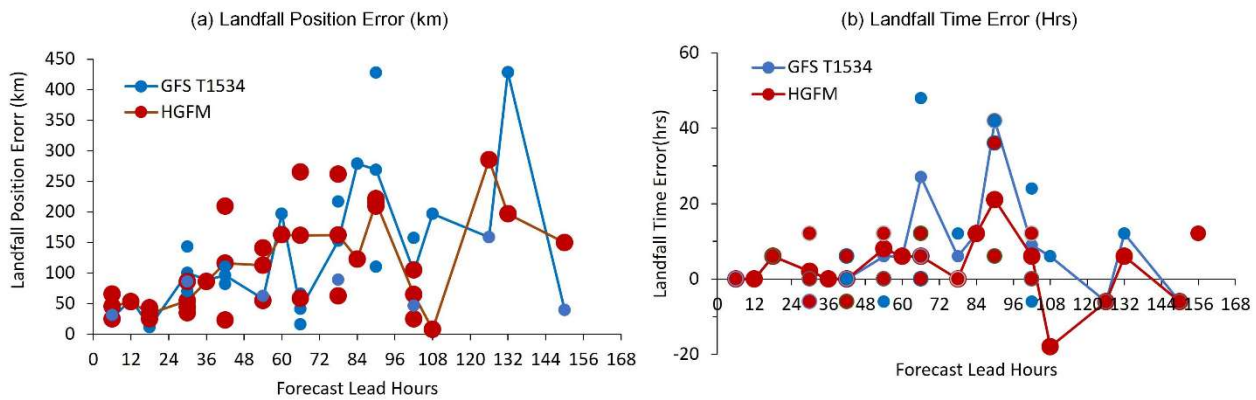


335

336 **Figure 11. a) RMSE of Track in km b) RMSE of MSW in kts c) Average Track error (km) d) Average Intensity Errors (kts).**



337

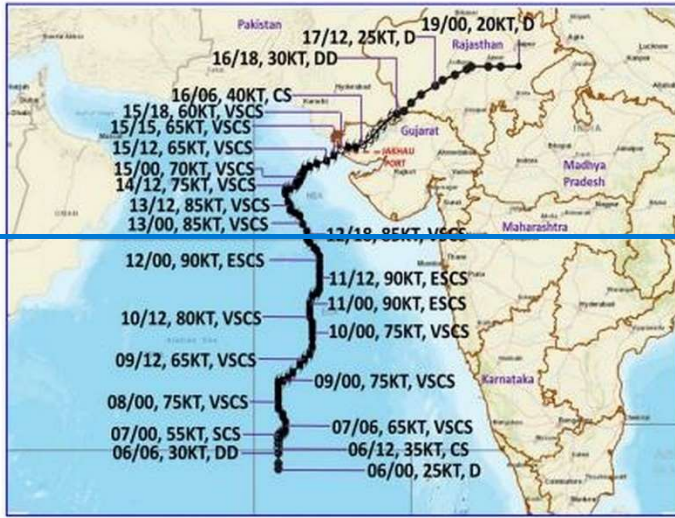


338

339 **Figure 12. a) Average Landfall position errors in km b) Average Landfall time Errors in hours. The continuous lines represent the**  
 340 **average errors for GFS T1534 (Blue) and HGFM (Red). The different size of the dots is for making the overlapped points visible.**

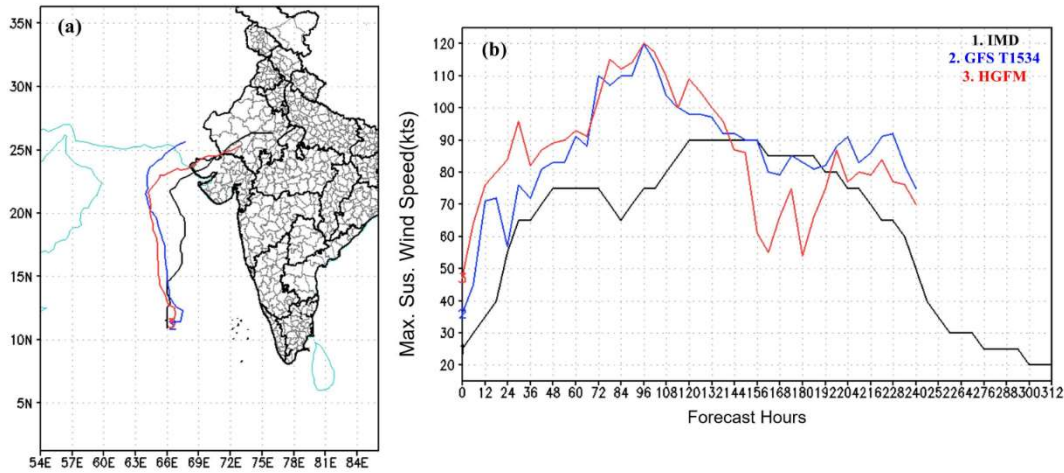
341 **3.5.2 A case study - Cyclone Biparjyo**

342 During the monsoon onset of 2023 season, tropical cyclone Biparjyo evolved in the Arabian Sea and hit the north-western  
 343 state of Gujarat, India. The cyclone Biparjyo lasted for quite a long--time during 6-19 June 2023. As seen in figure 13a, It  
 344 moved almost parallel to the Indian west coast and had a recurve to finally make landfall over the northern part of Gujarat  
 345 and adjoining Pakistan. It passed through the has rapid intensification during genesis and growing stage on 6 and 7 June its  
 346 life cycle. The observed track shown in Fig. 13 as provided by IMD. This case was particularly challenging for prediction  
 347 due to combination of recurving track, rapid intensification, slow movement and a long lifespan. The HGFM and GFS  
 348 T1534 track, and intensity forecast of TC Biparjyo based on 6 June (day of genesis) initial condition, is shown in Fig. 13 a  
 349 and b along with the best track data from IMD. It is evident that the HGFM -predicts a track much closer to the observation  
 350 compared to GFS T1534. Particularly the recurvature is better captured by HGFM at about 6-7 days lead time. Both the  
 351 models overestimated the intensity till 120 hrs of forecast and thereafter indicates dissipation phase.



- : LESS THAN 34 KT
- : 34-47 KT
- ⦿ : ≥ 48 KT
- D: Depression
- DD: Deep Depression
- CS: Cyclonic Storm
- SCS: Severe Cyclonic Storm
- VSCS: Very SCS
- ESCS: Extremely SCS
- : Observed Track

352



353

354

355 **Figure 13. (a) track and (b) intensity variation forecast by GFS T1534, HGFM and as reported by IMD for the case of Observed**  
 356 **track of Tropical cyclone Biparjoy over Arabian Sea during based on -6-19 June 2023 initial condition, as per India Meteorological**  
 357 **Department. Taken from open source: [https://rsmenewdelhi.imd.gov.in/report.php?internal\\_menu=Mjc=](https://rsmenewdelhi.imd.gov.in/report.php?internal_menu=Mjc=), page no. 90**

358 The HGFM and GFS T1534 track forecast of TC Biparjoy based on 6 June initial condition, is shown in Fig. 14. It is evident  
 359 that the HGFM generates a track much closer to the observation as compared to GFS T1534. The intensity expressed in  
 360 terms of maximum sustained wind has been computed and shown in Fig. 13 for 10 days (240 forecast hours). The intensity  
 361 of the TC appears to be overestimated by both the models till 120 hrs of forecast and thereafter the intensity seems to be  
 362 reasonably predicted with 6 June 0000 UTC initial condition. To know the robustness of the performance, the verification is



363 carried out for this particular case considering forecast from all the initial conditions. Both the models are tested with  
 364 different initial conditions (from 6 June 00UTC to 15 June 00UTC, every initialized at 24 hrs interval). A comparative  
 365 analysis of landfall position and landfall time errors with HGFM and GFS T1534 with respect to the observations obtained  
 366 that reported by from IMD has been mentioned in Table 2. It is evident that the landfall position error of the cyclone has  
 367 been significantly improved by HGFM forecast though the landfall time error appears to be almost equivalent as compared  
 368 to GFS T1534. Further the average track and intensity error (obtained from total 10 initial conditions) is depicted in Fig. 14a  
 369 and 14b. It is evident that the HGFM produces more consistently accurate prediction of track and intensity with lesser error  
 370 on longer lead while the errors are equivalent more or less same for shorter lead in the smaller lead.

371

372

373

374 **Table 2. Landfall position (km) and landfall time (hr) errors for the forecasts started with different initial conditions. -ve (+ve )**  
 375 **sign indicates early (late) landfall with respect to observed landfall time. The bold numbers indicates the significant improvement**  
 376 **in the landfall position errors with HGFM.**

Forecast Hours from Observed landfall (Hr)	Initial Condition	Landfall Position Error (km)		Landfall Time Error (Hr)		377
		GFS T1534	HGFM	GFS T1534	HGFM	378
228	2023060600	298	<b>57</b>	0	-30	379
204	2023060700	No Landfall				380
180	2023060800	616	<b>201</b>	0	0	381
156	2023060900	349	<b>197</b>	12	12	382
132	2023061000	428	<b>197</b>	12	6	383
108	2023061100	197	<b>7</b>	6	-18	384
84	2023061200	279	<b>123</b>	12	12	385
60	2023061300	197	<b>163</b>	6	6	386
36	2023061400	89	<b>86</b>	0	0	387
12	2023061500	57	<b>53</b>	0	0	388
						389
						390
						391
						392
						393
						394

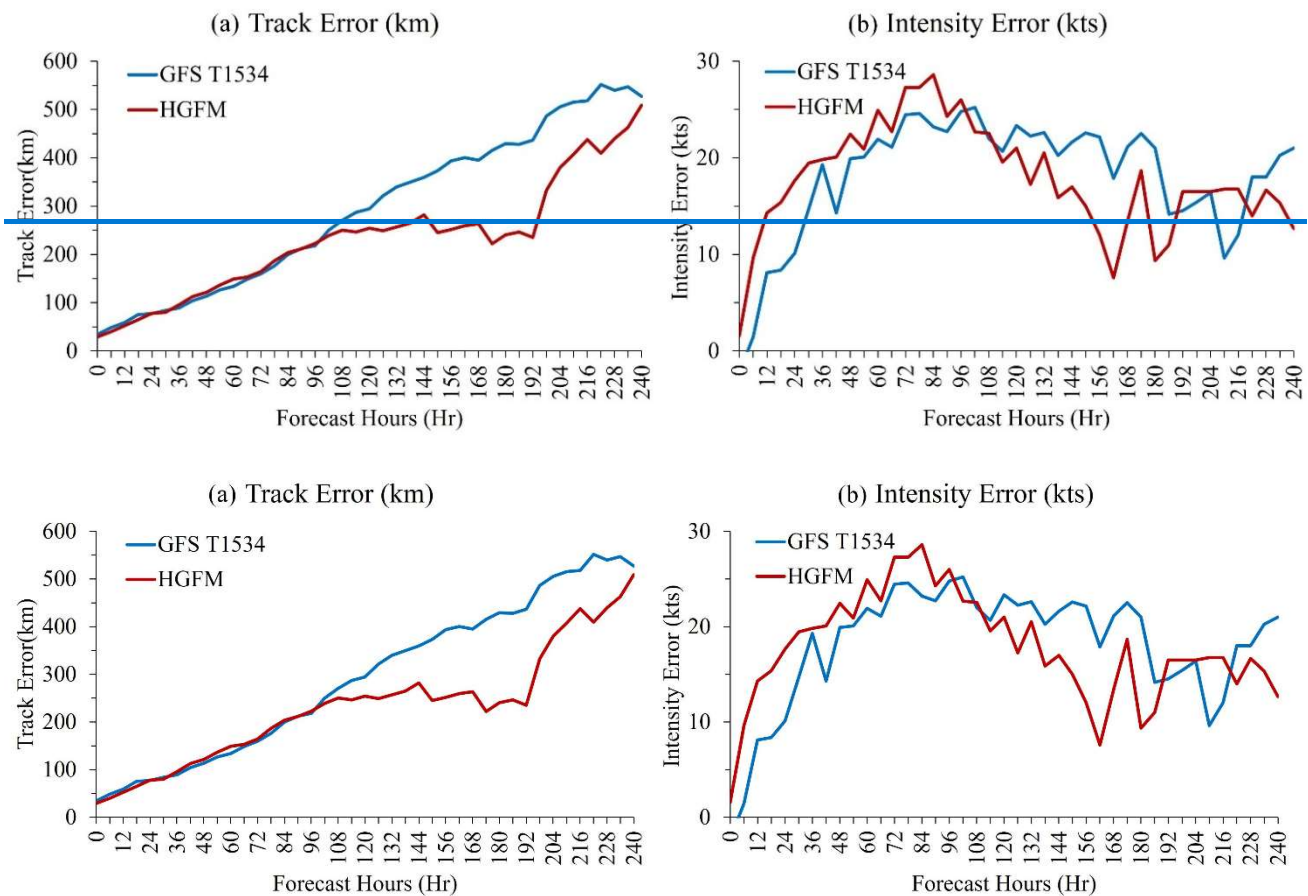


Figure 14. a) Average track error and b) average intensity error for the tropical cyclone Biparjoy over Arabian Sea.

#### 399 4 Conclusions

400 For the first time, a version of the GFS model utilizing a new grid structure triangular cubic octahedral (Tco) has been  
 401 developed and is being run on an experimental basis for short to medium range weather prediction over the Indian region,  
 402 designated as IITM High resolution Global Forecast Model (HGFM). The Tco grid provides a higher resolution over the  
 403 tropics, making the model achieve 6.5 km horizontal resolution near the tropics. This higher resolution represents a  
 404 substantial leap from the existing Gaussian linear GFS T1534 which maintains a resolution of 12.5 km across the globe. The  
 405 KE spectra of 200 hPa zonal wind have also revealed reasonable power by both the model with HGFM showing marginally  
 406 better power in the Kolmogorov region indicating fidelity of model structure.

407 ~~The HGFM being developed in the Tco grid provides many advantages, notably resolving the Gibbs phenomenon and~~  
 408 ~~spurious rain over mountainous regions has been resolved. It is worth to mention that the present dynamical core using cubic~~

409 octahedral grid is implemented in ECMWF weather forecast model since 2016 (Malardel et al., 2016). This has led to a  
410 significant increase in forecast accuracy and computational efficiency in the ECMWF model. In the present study, it is found  
411 that the above dynamical core in the GFS T1534 has improved the orographic rainfall and reduces the Gibbs noise over the  
412 mountainous region in addition to improved precipitation skill over the Indian landmass region. –The June-September  
413 monsoon rainfall and a case study of heavy rainfall have been analyzed in detail. The newly developed HGFM shows  
414 significantly better skill, particularly in the longer lead and for heavier rain categories. Rainfall biases over the whole globe  
415 appear to be broadly similar between HGFM and GFS T1534. A case of heavier rainfall in and around central India during  
416 the monsoon season has been analysed where the validation shows a significant gain in forecast lead time by the HGFM  
417 compared to GFS T1534. The HGFM captures rainfall signature at 5 days lead time, when there is hardly any indication in  
418 the HGFM model forecast.

419 Several cases of tropical cyclones during 2022 and 2023 were analysed, indicating better performance of HGFM compared  
420 to GFS in predicting tracks and intensity. A case of tropical cyclone Biparjoy has been evaluated in detail based on IMD  
421 observation. It is seen that the HGFM model generates better accuracy of cyclone position in almost all lead time (Table 2)  
422 and further the average track error also is found to be much lesser as compared to GFS T1534 in longer lead. However, the  
423 errors of both model in average track and intensity are found to be equivalent. This paper highlights the initial results of the  
424 newly developed HGFM model and its skill as compared to the operational GFS T1534 model. Subsequently more analyses  
425 for many events will be carried out and the model will be made operational for weather forecasts over India. The current set  
426 up of the model uses the same physics as the GFS model. However, the HGFM model would require some parameter tuning  
427 to optimize the performance of the model and increase its fidelity. The future work will be focused on detailed validation of  
428 model simulations with optimal set of physical parameterizations.

429

430

431

432

433

434

#### 435 **Code and Data Availability**

436 The model simulated data used for HGFM and GFS T1534 in the study are available at “TCO model data” by R Phani  
437 Murali Krishna, Kumar Siddharth, Athipatta Gopinathan Prajeesh, Malay Ganai, B. Revanth Reddy, Kumar Roy and  
438 Parthasarathi Mukhopadhyay, DOI: <https://doi.org/10.5281/zenodo.12569807>. The model code is available at "GFS TCO  
439 Model code" by R Phani Murali Krishna, Kumar Siddharth, Athipatta Gopinathan Prajeesh, Parthasarathi Mukhopadhyay.  
440 DOI: <https://doi.org/10.5281/zenodo.12526400>

441

442 **Author Contributions**

443 RPKM, SK, AGP and PM conceptualised the problem and made necessary changes/modification development of code for  
444 Tco and wrote the major part of the Introduction, data, methodology and over all sequences. PB and NW helped during  
445 formulation of the Tco grid in GFS and helped in improving the manuscript writing. KR, MG, ST, [BRR](#) and TG made all the  
446 forecast analysis of monsoon parameters and wrote the respective portion on analyses. RK, [MD and SS](#) made the analysis  
447 related to cyclone forecast by HGFm model and wrote the section on the cyclone forecast analysis and BRR made the  
448 dCAPE analysis and extracted the post processed variables for the analysis.

449

450

451 **Competing interests**

452 The authors declare that they have no conflict of interest.

453

454

455 **Disclaimer**

456

457

458

459 **Acknowledgments**

460 IITM is fully funded by the Ministry of Earth Sciences, Government of India. We would like to thank ECMWF for their  
461 support during the model development and for providing the ERA5 data set. We thank NCMRWF for providing the GFS  
462 initial conditions used for conducting simulations. We acknowledge Pratyush High Performance Computing at IITM, Pune  
463 for providing the computing facility to carry out the simulations. We thank Mr. Vaishak for helping in archiving the data in  
464 ARDC server. Authors thank Secretary Ministry of Earth Sciences, Government of India and Director, IITM for support and  
465 facilities provided for this study. We thank IMD for providing the [IMD](#)-GPM rainfall and cyclone best track data.

466

467

468 **References**

- 469 Abhik, S., Halder, M., Mukhopadhyay, P., Jiang, X., and Goswami, B.N.: A possible new mechanism for northward  
470 propagation of boreal summer intraseasonal oscillations based on TRMM and MERRA reanalysis, *Clim. Dyn.*, 40, 1611-  
471 1624, <https://doi.org/10.1007/s00382-012-1425-x>, 2013.
- 472 Abhik, S., Krishna, R.P.M., Mahakur, M., Ganai, M., Mukhopadhyay, P., and Dudhia, J.: Revised cloud processes to  
473 improve the mean and intraseasonal variability of Indian summer monsoon in climate forecast system: Part 1, *J. Adv.*  
474 *Model. Earth. Syst.*, 9(2), 1002-1029, <https://doi.org/10.1002/2016MS000819>, 2017.
- 475 Alpert, J.C., Kanamitsu, M., Caplan, P.M., Sela, J.G., White, G.H., and Kalnay, E.: Mountain induced gravity wave drag  
476 parameterization in the NMC medium-range forecast model. In Conference on Numerical Weather Prediction, Baltimore,  
477 MD, 8<sup>th</sup>, 726-733, 1988.
- 478 Arakawa, A. and Schubert, W.H.: Interaction of a cumulus cloud ensemble with the large-scale environment, Part I, *J.*  
479 *Atmos. Sci.*, 31(3), 674-701, [https://doi.org/10.1175/1520-0469\(1974\)031<0674:IOACCE>2.0.CO;2](https://doi.org/10.1175/1520-0469(1974)031<0674:IOACCE>2.0.CO;2), 1974.
- 480 Arakawa, A. and Wu, C.M.: A unified representation of deep moist convection in numerical modeling of the atmosphere.  
481 Part I, *J. Atmos. Sci.*, 70(7), 1977-1992, <https://doi.org/10.1175/JAS-D-12-0330.1>, 2013.
- 482 Bechtold, P., Köhler, M., Jung, T., Doblas-Reyes, F., Leutbecher, M., Rodwell, M. J., Vitart, F., and Balsamo, G.: Advances  
483 in simulating atmospheric variability with the ECMWF model: From synoptic to decadal time-scales, *Q. J. Roy. Meteor.*  
484 *Soc.*, 134, 1337–1351, <https://doi.org/10.1002/qj.289>, 2008.
- 485 Chattopadhyay, R., Goswami, B.N., Sahai, A.K., and Fraedrich, K.: Role of stratiform rainfall in modifying the northward  
486 propagation of monsoon intraseasonal oscillation, *J. Geophys. Res. Atmos.*, 114(D19),  
487 <https://doi.org/10.1029/2009JD011869>, 2009.
- 488 Choudhury, A.D. and Krishnan, R.: Dynamical response of the South Asian monsoon trough to latent heating from  
489 stratiform and convective precipitation, *J. Atmos. Sci.*, 68(6), 1347-1363, <https://doi.org/10.1175/2011JAS3705.1>, 2011.
- 490 Chun, H.Y. and Baik, J.J.: Momentum flux by thermally induced internal gravity waves and its approximation for large-scale  
491 models, *J. Atmos. Sci.*, 55(21), 3299-3310, [https://doi.org/10.1175/1520-0469\(1998\)055<3299:MFBTII>2.0.CO;2](https://doi.org/10.1175/1520-0469(1998)055<3299:MFBTII>2.0.CO;2), 1998.
- 492 Clough, S.A., Shephard, M.W., Mlawer, E.J., Delamere, J.S., Iacono, M.J., Cady-Pereira, K., Boukabara, S., and Brown,  
493 P.D.: Atmospheric radiative transfer modeling: A summary of the AER codes, *J. Quant. Spectrosc. Radiat. Transf.*, 91(2),  
494 233-244, <https://doi.org/10.1016/j.jqsrt.2004.05.058>, 2005.

495 Crueger, T., Giorgetta, M.A., Brokopf, R., Esch, M., Fiedler, S., Hohenegger, C., Kornblueh, L., Mauritsen, T., Nam, C.,  
496 Naumann, A.K., and Peters, K.: ICON-A, the atmosphere component of the ICON earth system model: II. Model evaluation,  
497 *J. Adv. Model. Earth. Syst.*, 10(7), 1638-1662, <https://doi.org/10.1029/2017MS001233>, 2018.

498 Deng, Q., Khouider, B., and Majda, A.J.: The MJO in a coarse-resolution GCM with a stochastic multcloud  
499 parameterization, *J. Atmos. Sci.*, 72(1), 55-74. <https://doi.org/10.1175/JAS-D-14-0120.1>, 2015.

500 Deshpande, M., Kanase, R., Krishna, R.P.M., Tirkey, S., Mukhopadhyay, P., Prasad, V.S., Johny, C.J., Durai, V.R., Devi, S.  
501 and Mohapatra, M.: Global Ensemble Forecast System (GEFS T1534) evaluation for tropical cyclone prediction over the  
502 North Indian Ocean, *Mausam.*, 72(1), 119-128, <https://doi.org/10.54302/mausam.v72i1.123>, 2021.

503 ECMWF IFS DOCUMENTATION—Cy43r1 Operational Implementation Part IV: Physical Processes; ECMWF: Reading,  
504 UK, 2016.

505 Fu, X. and Wang, B.: The boreal-summer intraseasonal oscillations simulated in a hybrid coupled atmosphere–ocean  
506 model, *Mon. Weather. Rev.*, 132(11), 2628-2649, <https://doi.org/10.1175/MWR2811.1>, 2004.

507 Gadgil, S. and Gadgil, S.: The Indian monsoon, GDP and agriculture, *Econ. polit. Wkly.*, 4887-4895,  
508 <https://www.jstor.org/stable/4418949>, 2006.

509 Ganai, M., Tirkey, S., Krishna, R.P.M., and Mukhopadhyay, P.: The impact of modified rate of precipitation conversion  
510 parameter in the convective parameterization scheme of operational weather forecast model (GFS T1534) over Indian  
511 summer monsoon region, *Atmos. Res.*, 248, 105185, <https://doi.org/10.1016/j.atmosres.2020.105185>, 2021.

512 Giorgetta, M.A., Brokopf, R., Crueger, T., Esch, M., Fiedler, S., Helmert, J., Hohenegger, C., Kornblueh, L., Köhler, M.,  
513 Manzini, E., and Mauritsen, T.: ICON-A, the atmosphere component of the ICON earth system model: I. Model description,  
514 *J. Adv. Model. Earth. Syst.*, 10(7), 1613-1637, <https://doi.org/10.1029/2017MS001242>, 2018.

515 Han, J. and Pan, H.L.: Revision of convection and vertical diffusion schemes in the NCEP Global Forecast System, *Weather.*  
516 *Forecast.*, 26(4), 520-533, <https://doi.org/10.1175/WAF-D-10-05038.1>, 2011.

517 Han, J., Witek, M.L., Teixeira, J., Sun, R., Pan, H.L., Fletcher, J.K., and Bretherton, C.S.: Implementation in the NCEP GFS  
518 of a hybrid eddy-diffusivity mass-flux (EDMF) boundary layer parameterization with dissipative heating and modified stable  
519 boundary layer mixing, *Weather. Forecast.*, 31(1), 341-352, <https://doi.org/10.1175/WAF-D-15-0053.1>, 2016.

- 520 Han, J., Wang, W., Kwon, Y.C., Hong, S.Y., Tallapragada, V., and Yang, F.: Updates in the NCEP GFS cumulus convection  
521 schemes with scale and aerosol awareness, *Weather. Forecast.*, 32(5), 2005-2017, [https://doi.org/10.1175/WAF-D-17-](https://doi.org/10.1175/WAF-D-17-0046.1)  
522 0046.1, 2017.
- 523 Held, I.M. and Suarez, M.J.: A proposal for the intercomparison of the dynamical cores of atmospheric general circulation  
524 models, *Bull. Am. Meteorol. Soc.*, 75(10), 1825-1830, [https://doi.org/10.1175/1520-](https://doi.org/10.1175/1520-0477(1994)075<1825:APFTIO>2.0.CO;2)  
525 0477(1994)075<1825:APFTIO>2.0.CO;2, 1994.
- 526 Hersbach, H. and Dee, D.: ERA5 reanalysis is in production. ECMWF Newsletter No. 147,  
527 ECMWF, Reading, United Kingdom, 7, [http://www.ecmwf.int/sites/default/files/elibrary/2016/16299-newsletter-no147-spring-](http://www.ecmwf.int/sites/default/files/elibrary/2016/16299-newsletter-no147-spring-2016.pdf)  
528 2016.pdf, 2016.
- 529 Hoffman, R.N., Kumar, V.K., Boukabara, S.A., Ide, K., Yang, F., and Atlas, R.: Progress in forecast skill at three leading  
530 global operational NWP centers during 2015–17 as seen in summary assessment metrics (SAMs), *Weather. Forecast.*, 33(6),  
531 1661-1679, <https://doi.org/10.1175/WAF-D-18-0117.1>, 2018.
- 532 Huffman, G.J., Stocker, E.F., Bolvin, D.T., Nelkin, E.J., and Tan, J.: GPM IMERG Final Precipitation L3 Half Hourly 0.1  
533 degree x 0.1 degree V06, Greenbelt, MD, Goddard Earth Sciences Data and Information Services Center (GES DISC),  
534 Accessed: 20 March 2023, doi:10.5067/GPM/IMERG/3B-HH/06, 2019.
- 535 Iacono, M.J., Mlawer, E.J., Clough, S.A., and Morcrette, J.J.: Impact of an improved longwave radiation model, RRTM, on  
536 the energy budget and thermodynamic properties of the NCAR community climate model, CCM3, *J. Geophys. Res. Atmos.*,  
537 105(D11), 14873-14890, <https://doi.org/10.1029/2000JD900091>, 2000.
- 538 Jiang, X., Li, T., and Wang, B.: Structures and mechanisms of the northward propagating boreal summer intraseasonal  
539 oscillation, *J. Clim.*, 17(5), 1022-1039, [https://doi.org/10.1175/1520-0442\(2004\)017<1022:SAMOTN>2.0.CO;2](https://doi.org/10.1175/1520-0442(2004)017<1022:SAMOTN>2.0.CO;2), 2004.
- 540 [Kanase, R., Tirkey, S., Deshpande, M., Krishna, R.-P.-M., Johny, C.-J., Mukhopadhyay, P., Iyengar, G., and Mohapatra, M.:](#)  
541 [Evaluation of the Global Ensemble Forecast System \(GEFS T1534\) for the probabilistic prediction of cyclonic disturbances](#)  
542 [over the North Indian Ocean during 2020 and 2021, \*J. Earth. Sys. Sci.\*, \*\*enees\*\* 132-143, \[https://doi.org/10.1007/s12040-023-\]\(https://doi.org/10.1007/s12040-023-02166-2\)](#)  
543 [02166-2](#), 2023.
- 544 Kim, Y.J. and Arakawa, A.: Improvement of orographic gravity wave parameterization using a mesoscale gravity wave  
545 model, *J. Atmos. Sci.*, 52(11), 1875-1902, [https://doi.org/10.1175/1520-0469\(1995\)052<1875:IOOGWP>2.0.CO;2](https://doi.org/10.1175/1520-0469(1995)052<1875:IOOGWP>2.0.CO;2), 1995.

546 [Kinter, J.L., Cash, B., Achuthavarier, D., Adams, J., Altshuler, E., Dirmeyer, P., Doty, B., Huang, B., Jin, E.K., Marx, L.,](#)  
547 [and Manganello, J.: Revolutionizing climate modeling with Project Athena: a multi-institutional, international collaboration,](#)  
548 [Bull. Am. Meteorol. Soc., 94\(2\), 231-245, <https://doi.org/10.1175/BAMS-D-11-00043.1>, 2013.](#)

549 [Kinter, J. L., III, Cash, B., Achuthavarier, D., Adams, J., Altshuler, E., Dirmeyer, P., Doty, B., Huang, B., Jin, E. K., Marx,](#)  
550 [L., Manganello, J., Stan, C., Wakefield, T., Palmer, T., Hamrud, M., Jung, T., Miller, M., Towers, P., Wedi, N., Satoh, M.,](#)  
551 [Tomita, H., Kodama, C., Nasuno, T., Oouchi, K., Yamada, Y., Taniguchi, H., Andrews, P., Baer, T., Ezell, M., Halloy, C.,](#)  
552 [John, D., Loftis, B., Mohr, R., & Wong, K.: Revolutionizing Climate Modeling with Project Athena: A Multi-Institutional,](#)  
553 [International Collaboration. Bull. Am. Meteorol. Soc., 94\(2\), 231-245. <https://doi.org/10.1175/BAMS-D-11-00043.1>, 2013.](#)

554 Kumar, S., Arora, A., Chattopadhyay, R., Hazra, A., Rao, S.A., and Goswami, B.N.: Seminal role of stratiform clouds in  
555 large-scale aggregation of tropical rain in boreal summer monsoon intraseasonal oscillations, *Clim. Dyn.*, 48, 999-1015,  
556 <https://doi.org/10.1007/s00382-016-3124-5>, 2017.

557 Kumar, S., Phani, R., Mukhopadhyay, P., and Balaji, C.: Does increasing horizontal resolution improve seasonal prediction  
558 of Indian summer monsoon?: A climate forecast system model perspective, *Geophys. Res. Lett.*, 49(7), e2021GL097466,  
559 <https://doi.org/10.1029/2021GL097466>, 2022.

560 [Li, J., Yu, R., Yuan, W., Chen, H., Sun, W. and Zhang, Y.: Precipitation over East Asia simulated by NCAR CAM5 at](#)  
561 [different horizontal resolutions. \*J. Adv. Model. Earth. Syst.\*, 7\(2\), 774-790, <https://doi.org/10.1002.2014MS000414>, 2015.](#)

562 Lott, F. and Miller, M.J.: A new subgrid-scale orographic drag parametrization: Its formulation and testing, *Q. J. R.*  
563 *Meteorol. Soc.*, 123(537), 101-127, <https://doi.org/10.1002/qj.49712353704>, 1997.

564 Magnusson, L. and Källén, E.: Factors influencing skill improvements in the ECMWF forecasting system, *Mon. Weather.*  
565 *Rev.*, 141(9), 3142-3153, <https://doi.org/10.1175/MWR-D-12-00318.1>, 2013.

566 [Majewski, D., Liermann, D., Prohl, P., Ritter, B., Buchhold, M., Hanisch, T., Paul, G., Wergen, W. and Baumgardner, J.:](#)  
567 [The operational global icosahedral-hexagonal gridpoint model GME: description and high resolution tests, \*Mon. Wea. Rev.\*,](#)  
568 [130, 319– 338, \[https://doi.org/10.1175/1520-0493\\(2002\\)130<0319:TOGIHG>2.0.CO;2\]\(https://doi.org/10.1175/1520-0493\(2002\)130<0319:TOGIHG>2.0.CO;2\), 2002.](#)

569 [Malardel, S., N. Wedi., W. Deconinck., M. Diamantakis., C. Kühnlein., G. Mozdzyński., M. Hamrud. and P.](#)  
570 [Smolarkiewicz.: A new grid for the IFS, ECMWF Newsletter No. 146, 23–28, 2016.](#)

571 Mitra, A.K., Prakesh, S., Imranali, M.M., Pai, D.S. and Srivastava, A.K.: Daily merged satellite gauge real-time rainfall  
572 dataset for Indian Region, *Vayumandal*, 40(1-4), 33-43, 2014.



573 Miura, H., Satoh, M., Nasuno, T., Noda, A. T., and Oouchi, K.: A Madden-Julian Oscillation event realistically simulated by  
574 a global cloud-resolving model, *Sci.*, 318(5857), 1763–1765, <https://doi.org/10.1126/science.1148443>, 2007.

575 Molod, A., Takacs, L., Suarez, M., and Bacmeister, J.: Development of the GEOS-5 atmospheric general circulation model:  
576 Evolution from MERRA to MERRA2, *Geosci. Model. Dev.*, 8(5), 1339-1356, <https://doi.org/10.5194/gmd-8-1339-2015>,  
577 2015.

578 Mukhopadhyay, P., Prasad, V.S., Krishna, R.P.M., Deshpande, M., Ganai, M., Tirkey, S., Sarkar, S., Goswami, T., Johny,  
579 C.J., Roy, K., and Mahakur, M.: Performance of a very high-resolution global forecast system model (GFS T1534) at 12.5  
580 km over the Indian region during the 2016–2017 monsoon seasons, *J. Earth Sys. Sci.*, 128, 1-18,  
581 <https://doi.org/10.1007/s12040-019-1186-6>, 2019.

582 Mukhopadhyay, P., Bechtold, P., Zhu, Y., Murali Krishna, R.P., Kumar, S., Ganai, M., Tirkey, S., Goswami, T., Mahakur,  
583 M., Deshpande, M., and Prasad, V.S.: Unraveling the mechanism of extreme (more than 30 sigma) precipitation during  
584 August 2018 and 2019 over Kerala, India, *Weather. Forecast.*, 36(4), 1253-1273, <https://doi.org/10.1175/WAF-D-20-0162.1>,  
585 2021.

586 Nastrom, G.D. and Gage, K.S.: A climatology of atmospheric wavenumber spectra of wind and temperature observed by  
587 commercial aircraft, *J. Atmos. Sci.*, 42, 950–960, [https://doi.org/10.1175/1520-0469\(1985\)042<0950:ACOAWS>2.0.CO;2](https://doi.org/10.1175/1520-0469(1985)042<0950:ACOAWS>2.0.CO;2),  
588 1985.

589 Pan, H.L. and Wu, W.S.: Implementing a mass flux convection parameterization package for the NMC medium-range  
590 forecast model. <https://repository.library.noaa.gov/view/noaa/11429>, 1995.

591 Prakash, S., Mitra, A.K., Momin, I.M., Rajagopal, E.N., Milton, S.F., and Martin, G.M.: Skill of short-to medium-range  
592 monsoon rainfall forecasts from two global models over India for hydro-meteorological applications, *Meteorol. Appl.*, 23(4),  
593 574-586, <https://doi.org/10.1002/met.1579>, 2016.

594 Prasad, V.S., Mohandas, S., Gupta, M.D., Rajagopal, E.N., and Dutta, S.K.: Implementation of upgraded global forecasting  
595 systems (T382L64 and T574L64) at NCMRWF, In NCMRWF Technical Report, 1-72, 2011.

596 Prasad, V.S., Mohandas, S., Dutta, S.K., Gupta, M.D., Iyengar, G.R., Rajagopal, E.N., and Basu, S.: Improvements in  
597 medium range weather forecasting system of India, *J. Earth. Sys. Sci.*, 123, 247-258, <https://doi.org/10.1007/s12040-014->  
598 0404-5, 2014.

599 Prasad, V.S., Johny, C.J., Mali, P., Singh, S.K., and Rajagopal, E.N.: Global retrospective analysis using NGFS for the  
600 period 2000–2011, *Current Sci.*, 370-377, <https://www.jstor.org/stable/24912364>, 2017.

601 Rajendran, K., Kitoh, A., Mizuta, R., Sajani, S., and Nakazawa, T.: High-resolution simulation of mean convection and its  
602 intraseasonal variability over the tropics in the MRI/JMA 20-km mesh AGCM, *J. Clim.*, 21(15), 3722-3739,  
603 <https://doi.org/10.1175/2008JCLI1950.1>, 2008.

604 Rao, S.A., Goswami, B.N., Sahai, A.K., Rajagopal, E.N., Mukhopadhyay, P., Rajeevan, M., Nayak, S., Rathore, L.S.,  
605 Sheno, S.S.C., Ramesh, K.J., and Nanjundiah, R.S.: Monsoon mission: a targeted activity to improve monsoon prediction  
606 across scales, *Bull. Am. Meteorol. Soc.*, 100(12), 2509-2532, <https://doi.org/10.1175/BAMS-D-17-0330.1>, 2019.

607 [Raymond, D. J.: Convection in the east Pacific Intertropical Convergence Zone, \*Geophys. Res. Lett.\*, 44, 562-568,](#)  
608 [doi:10.1002/2016GL071554](https://doi.org/10.1002/2016GL071554), 2017.

609 RSMC Report, Report on Cyclonic disturbances over North Indian Ocean during 2022, India Meteorological Department,  
610 [https://rsmcnewdelhi.imd.gov.in/report.php?internal\\_menu=Mjc=](https://rsmcnewdelhi.imd.gov.in/report.php?internal_menu=Mjc=)

611 RSMC Report, Report on Cyclonic disturbances over North Indian Ocean during 2023, India Meteorological Department,  
612 [https://rsmcnewdelhi.imd.gov.in/report.php?internal\\_menu=Mjc=](https://rsmcnewdelhi.imd.gov.in/report.php?internal_menu=Mjc=)

613 Satoh, M., Tomita, H., Miura, H., Iga, S., and Nasuno, T.: Development of a global cloud resolving model-a multi-scale  
614 structure of tropical convections, *J. Earth. Simul.*, 3, 11-19, 2005.

615 Satoh, M., Stevens, B., Judt, F., Khairoutdinov, M., Lin, S.J., Putman, W.M., and Düben, P.: Global cloud-resolving models,  
616 *Curr. Clim. Change Rep.*, 5, 172-184, <https://doi.org/10.1007/s40641-019-00131-0>, 2019.

617 [Skamarock, W.C.: Evaluating Mesoscale NWP Models Using Kinetic Energy Spectra, \*Mon. Weather. Rev.\*, 132,3019–3032,](#)  
618 <https://doi.org/10.1175/MWR2830.1>, 2004.

619 Skamarock, W.C., Klemp, J.B., Duda, M.G., Fowler, L.D., Park, S.H., and Ringler, T.D.: A multiscale nonhydrostatic  
620 atmospheric model using centroidal Voronoi tessellations and C-Grid staggering, *Mon. Weather. Rev.*, 140(9), 3090–  
621 3105, <https://doi.org/10.1175/MWR-D-11-00215.1>, 2012.

622 [Staniforth, A. and Thuburn, J.: Horizontal grids for global weather and climate prediction models: a review. \*Q. J. R.\*](#)  
623 [Meteorol. Soc.](https://doi.org/10.1002/qj.958), 138(662), 1-26, <https://doi.org/10.1002/qj.958>, 2012.

624 Stephens, G.L., L'Ecuyer, T., Forbes, R., Gettelmen, A., Golaz, J.C., Bodas-Salcedo, A., Suzuki, K., Gabriel, P., and Haynes,  
625 J.: Dreary state of precipitation in global models, *J. Geophys. Res. Atmos.*, 115(D24), <https://doi.org/10.1029/2010JD014532>,  
626 2010.

627 Sundqvist, H., Berge, E., and Kristjánsson, J.E.: Condensation and cloud parameterization studies with a mesoscale  
628 numerical weather prediction model, *Mon. Weather. Rev.*, 117(8), 1641-1657, <https://doi.org/10.1175/1520->  
629 0493(1989)117<1641:CACPSW>2.0.CO;2, 1989.

630 Watson, P.A., Berner, J., Corti, S., Davini, P., von Hardenberg, J., Sanchez, C., Weisheimer, A., and Palmer, T.N.: The  
631 impact of stochastic physics on tropical rainfall variability in global climate models on daily to weekly time scales, *J.*  
632 *Geophys. Res. Atmos.*, 122(11), 5738-5762, <https://doi.org/10.1002/2016JD026386>, 2017.

633 Wedi, N.P., Polichtchouk, I., Dueben, P., Anantharaj, V.G., Bauer, P., Boussetta, S., Browne, P., Deconinck, W., Gaudin,  
634 W., Hadade, I., and Hatfield, S.: A baseline for global weather and climate simulations at 1 km resolution, *J. Adv. Model.*  
635 *Earth. Syst.*, 12(11), e2020MS002192, <https://doi.org/10.1029/2020MS002192>, 2020.

636 Westra, S., Fowler, H.J., Evans, J.P., Alexander, L.V., Berg, P., Johnson, F., Kendon, E.J., Lenderink, G., and Roberts, N.:  
637 Future changes to the intensity and frequency of short-duration extreme rainfall, *Rev. Geophys.*, 52(3), 522-555,  
638 <https://doi.org/10.1002/2014RG000464>, 2014.

639 Zhang, G.J.: Convective quasi-equilibrium in the tropical western Pacific: Comparison with midlatitude continental  
640 environment, *J. Geophys. Res. Atmos.*, 108(D19), <https://doi.org/10.1029/2003JD003520>, 2003.

641 Zhao, Q. and Carr, F.H.: A prognostic cloud scheme for operational NWP models, *Mon. Weather. Rev.*, 125(8), 1931-1953,  
642 [https://doi.org/10.1175/1520-0493\(1997\)125<1931:APCSFO>2.0.CO;2](https://doi.org/10.1175/1520-0493(1997)125<1931:APCSFO>2.0.CO;2), 1997.